LA-SUB--95-102

MRC/ABQ-R-1686
Copy 2

Mission Research Corporation

COMPUTATIONAL SUPPORT FOR ITS AND PHERMEX

Final Report

Thomas P. Hughes
Robert E. Clark
Mission Research Corporation

Paul W. Allison
David C. Moir
Todd J. Kauppila
Scott A. Watson
Los Alamos National Laboratory

March 1994

Prepared for: LOS ALAMOS NATIONAL LABORATORY
Post Office Box 1663
Los Alamos, NM 87545

Under Contract: 9-XQ2-7754F-1

Prepared by: MISSION RESEARCH CORPORATION
1720 Randolph Road, SE.
Albuquerque, NM 87106-4245
(505) 768-7600

DISCLAIMER

Portions of this document may be illegible in electronic image products. Images are produced from the best available original document.

CONTENTS

CONTENTS (CONTINUED)

FIGURES

FIGURES (CONTINUED)

FIGURES (CONTINUED)

FIGURES (CONTINUED)

FIGURES (CONTINUED)

1.0 SUMMARY

This report describes calculations carried out over the past year in support of the ITS and PHERMEX radiographic machines. The main results are as follows.

ITS: The forces produced by nonaxisymmetric structures in the ITS linac were calculated using 3-D simulations. The quadrupole magnetic field produced by the drive rods in the accelerating cell was obtained (Sec. 2.1). This force can be corrected by a weak static magnetic quadrupole provided the current in the drive rods is constant. The octopole force produced by a 4-hole diagnostic section was also obtained (Sec. 2.2).

A new recessed cathode design was modeled using PBGUNS. For a 2 mm recess, the electrostatic focusing due to the recess is sufficient to stop current loss on the anode (Sec. 2.3). The emitted and transported currents are in good agreement with the measured values. This is an improvement on flush-cathode results previously reported, where there was a significant discrepancy between calculated and measured current.

The LAMDA code was compared in detail to the LLNL code BREAKUP (Sec. 2.4). The codes are in close agreement. To get the results to overlay identically, however, the beam voltages have to differ by about 100 kV (out of 3 MV). The source of this discrepancy has not yet been identified.

A plotting utility for LAMDA was written in the IDL® language (Sec. 4.1). This allows LAMDA output to be viewed on any platform supported by IDL.

PHERMEX: Experiments on the flat-cathode injector were modeled. Beam radius as a function of magnet strength was compared in detail with measurements, and good agreement was obtained (Sec. 3.1).

The effect of the trim coil on reducing beam emittance was investigated further (Sec. 3.2). The trim coil allows one to correct emittance growth due to spherical aberration in the focusing magnet and nonlinear self forces.

The measured calibrations for the bucking, focus and trim coils are now in good agreement with the calculated values (Sec. 3.1).

A code which optimizes the transport magnet settings was developed. The code iterates on the magnet settings to obtain a beam envelope with some user-specified properties (Sec. 3.3). This procedure may be useful in tuning the ITS or DARHT linacs.

2.0 ITS CALCULATIONS

2.1 Quadrupole Field in the DARHT Accelerating Cell

The DARHT accelerating cell is connected to the pulsed power by two radial drive rods. During the flat-top of the accelerating pulse, these rods conduct a total current equal to the sum of the beam current and leakage current. We have used a 3-D electromagnetic field solver to compute the non-axisymmetric fields produced in the beam-pipe when the leakage current is zero. (The results can be scaled to include the leakage current.)

We find that, out to a radius of about 3 cm, the dominant field is a quadrupole with $\int \partial B_y/\partial x \; dz \approx 2.3$ gauss. This is about a factor of 5 higher than results obtained from MAFIA, but is in line with analytic estimates. When the effect of ferrite is included, the quadrupole strength increases to 3 gauss. We have checked our code against the analytic results of Gluckstern and Cooper for a simple geometry and obtain good agreement.

The quadrupole field can be corrected with a static magnetic quadrupole to the extent that the current in the drive rods is constant during the main part of the beam pulse.

2.1.1 Geometry

A sketch of the accelerating cell is shown in Fig. 1. The two drive rods which feed the pulsed power to the cell are 180 degrees apart. We used the 3-D gridded field solver BTEC (Refs. 1, 2) to model the problem. For initial runs, the geometry, shown in Fig. 2, was approximately the same as that used in MAFIA calculations (Ref. 3). A section of the grid is shown in Fig. 2b. In this geometry, the ferrite region was represented by a perfect conductor. Wave-transmitting boundary conditions were applied at the left and right boundaries. Later, we modified the geometry to put in a ferrite region with $\mu = 250$, as shown in Fig. 3. The grid resolution in each case was $\Delta z = 0.2857$ cm, $\Delta x = 0.285$ cm $= \Delta y$. Our initial simulation attempts used nonuniform zoning to reduce memory requirements, but produced some anomalous results (viz. large differences in the quadrupole gradients in the x and y directions). The results given below used uniform zoning.

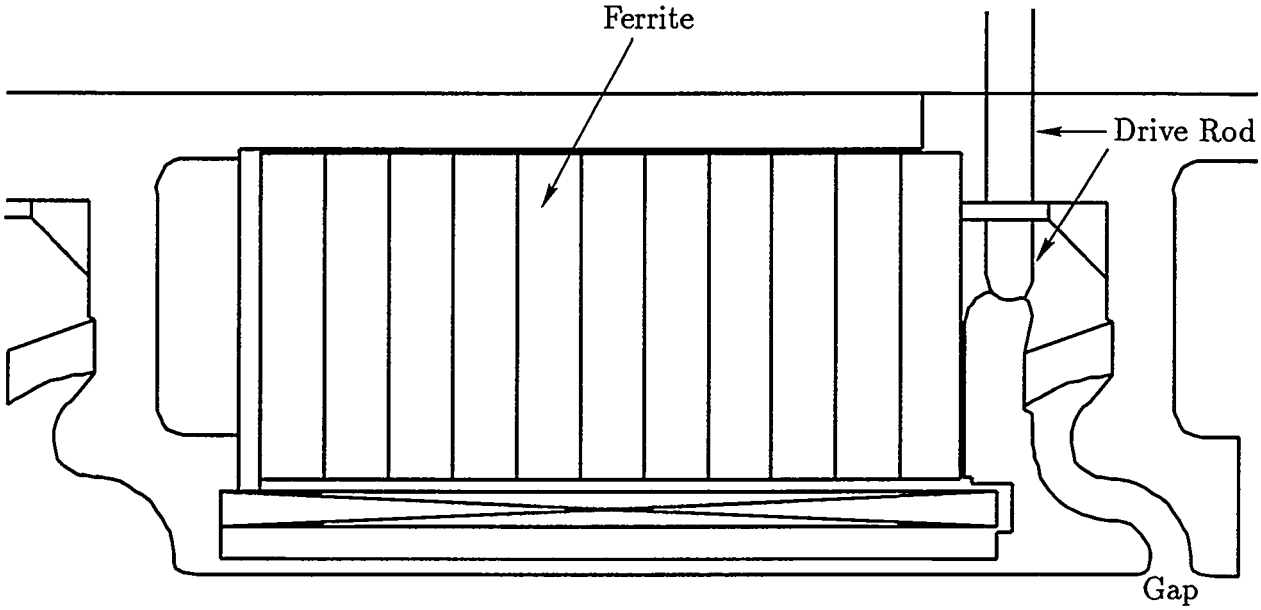

Figure 1. Schematic of DARHT accelerating cell showing drive rods, ferrite and shielded gap geometry. (From Drawing No. 47Y274728.)

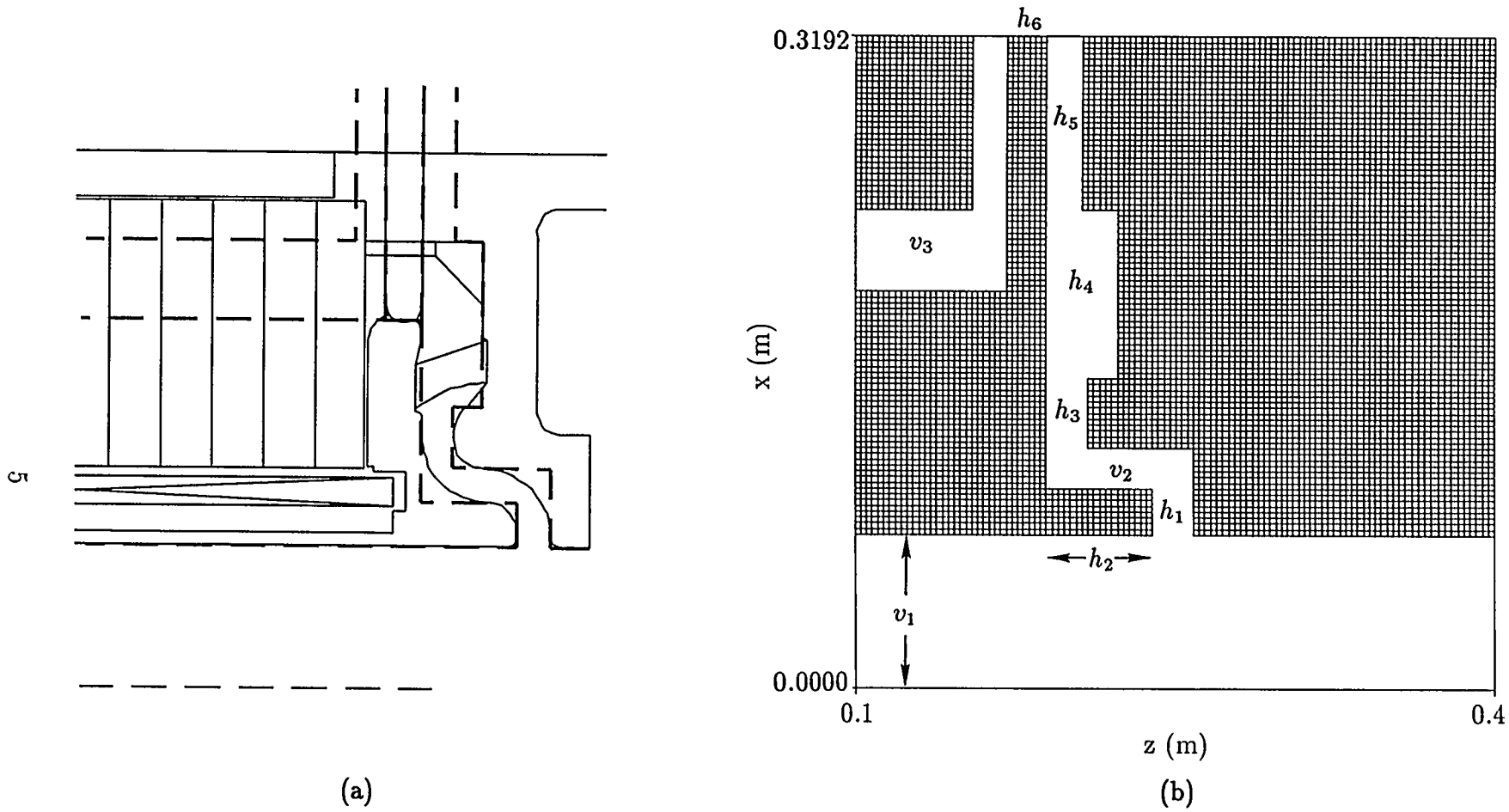

Figure 2. Simplified gap geometry, outlined by dashed line, used in MAFIA and initial BTEC calculations is shown in (a). Frame (b) shows a section of the BTEC grid. Vertical dimensions (cm) are: $v_1 = 7.4$, $v_2 = 2$, $v_3 = 4.0$. Horizontal dimensions (cm) are $h_1 = 2$, $h_2 = 5.14$, $h_3 = 2$, $h_4 = 3.43$, $h_5 = 1.7$, $h_6 = 2$. Cell size is $\Delta x = 0.2850$ cm $= \Delta y$, $\Delta z = 0.2857$ cm.

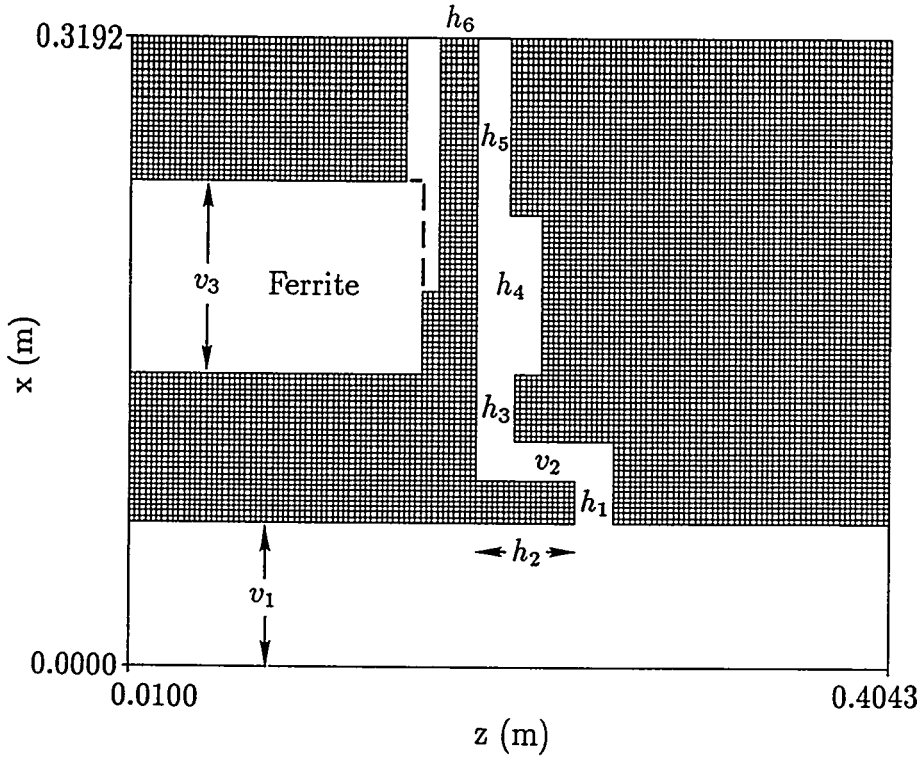

Figure 3. Modified BTEC grid with ferrite region. Dimensions are same as in Fig. 2b except $v_3 = 9.975$ cm.

2.1.2 Field Calculation

The fields we wish to calculate are the quasi steady-state fields that exist during the flat-top of the beam current pulse. During this time, the drive rods conduct a current equal to the sum of the beam current and the leakage current. Cell measurements made some time ago indicate that the leakage current has an approximately constant value of about 1000 A (Ref. 4) (see Appendix A). This means that each drive rod carries a current of about $(3000 + 1000)/2$ A. In the following, we do not include the leakage current, but the results can be simply scaled to take it into account.

To obtain the fields produced by the current in the drive rods using BTEC, we drive a current along the axis of the beam pipe in Fig. 2b, and slowly ramp it in time to a value of 3 kA. "Slow" here means on a time scale long compared to the period of RF resonances of the accelerating gap, which we do not wish to excite. For the DARHT cell, the lowest RF

resonances have a period of about 3.3 ns (Ref. 5). The temporal profile of the drive current is shown in Fig. 4a. Figure 4b shows that a return current equal to the beam current flows in the drive rods. We calculate instantaneous integrals of the transverse Lorentz force along the beam pipe, viz.,

$$W(t) = e \int (\mathbf{E}_\perp - v_z \hat{z} \times \mathbf{B}_\perp)\, dz \tag{1}$$

where e is the electronic charge. The integral is taken over a 25 cm length centered on the gap. To isolate the weak non-axisymmetric fields from the strong axisymmetric self-fields of the beam, we use a current traveling at the velocity of light to excite the structure, and use $v_z = c$ in Eq. 1. In this situation, $W(t)$ is zero in a straight pipe, because the electric and magnetic forces cancel exactly. We compute $W(t)$ at a number of points along the x- and y-axes. (The drive-rods are along the x-axis.) As shown in Fig. 5, $W(t)$ oscillates about a mean value due to low-level RF modes. We average over these oscillations to obtain the steady-state field value. The values are plotted versus radius in Fig. 6. Out to a radius of about 3 cm, the curves have a constant slope, indicating a quadrupole field component, as expected. The magnitudes of the two slopes, obtained by fitting a straight line to the first three points on each curve, differ by about 10% indicating some numerical error. In the MAFIA calculations (Ref. 3), the two slopes differed by a factor of 4. (BTEC also gave large differences when nonuniform zoning was used; we do not know whether nonuniform zoning was used in MAFIA.)

The focusing strength of the quadrupole is given by the quantity

$$\int \left(\frac{\partial B_y}{\partial x} \right) dz \approx 2.3 \text{ gauss} \tag{2}$$

where we have used the average of the two slopes. (The slopes in Fig. 6 are divided by 300 to get units of gauss). In the MAFIA calculations, quadrupole strengths of 0.12 and 0.5 gauss were measured. We suspect that in MAFIA, the drive rods were not conducting the full beam current. Some current may have been flowing down the left-hand boundary and across the top of the "ferrite". Since real ferrite is a poor conductor, there is little current flow along this path in the real cell. In BTEC, the left-hand-side boundary conditions did not allow current to flow along the top of the "ferrite".

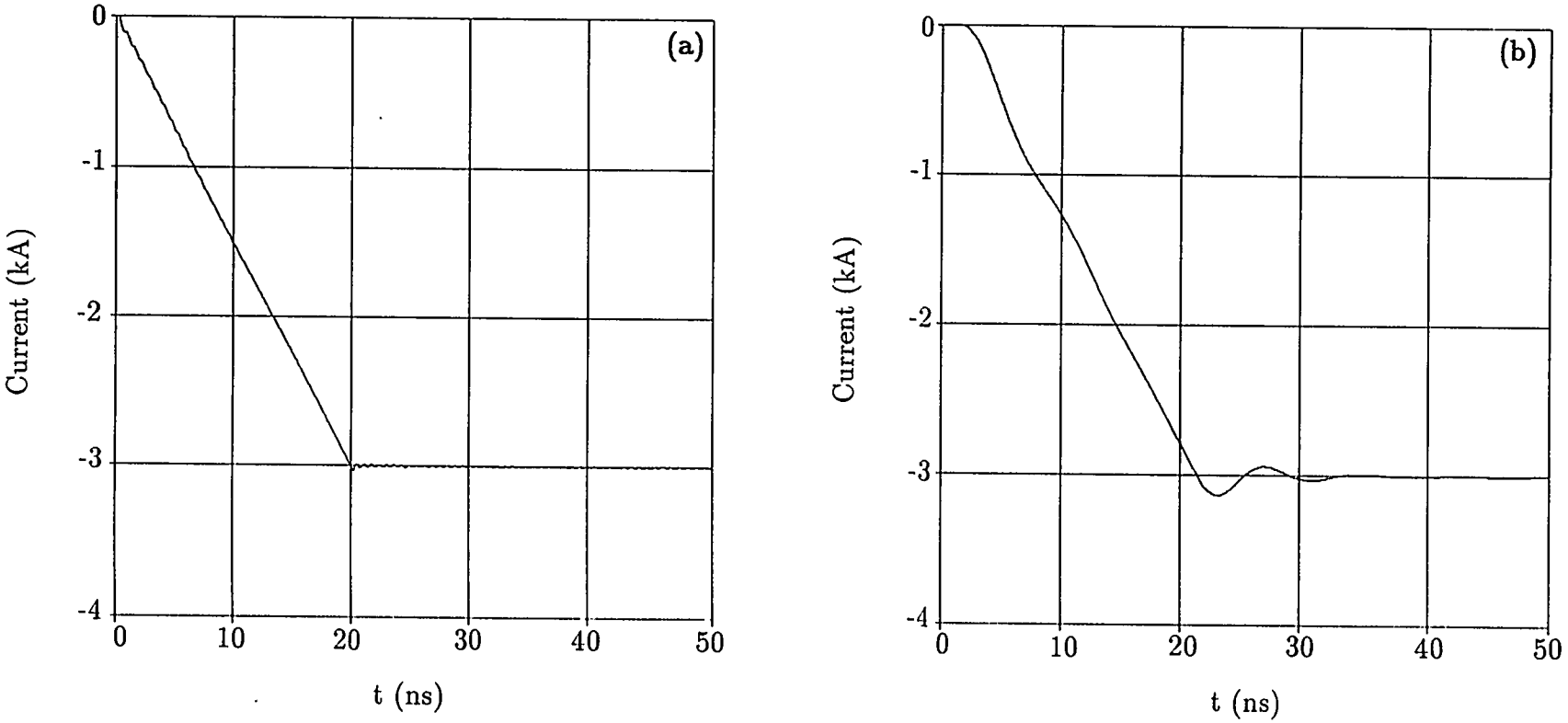

Figure 4. Temporal profiles of (a) injected axial beam current, (b) drive-rod current. (Run L14).

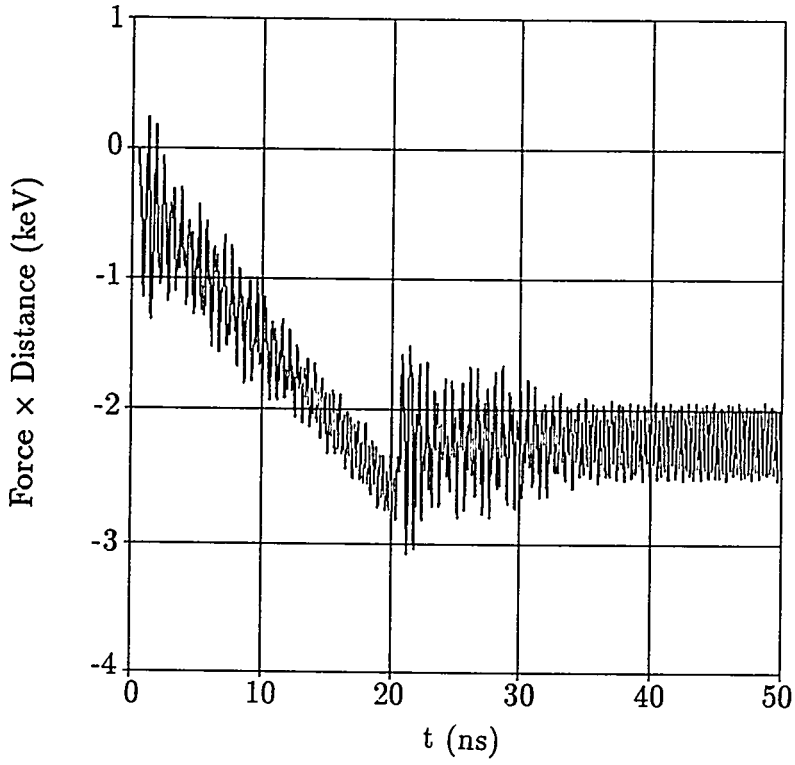

Figure 5. Temporal variation of integrated transverse force at $x = 3$ cm, $y = 0 = z$. RF oscillations are averaged over to get steady-state value. (Run L12).

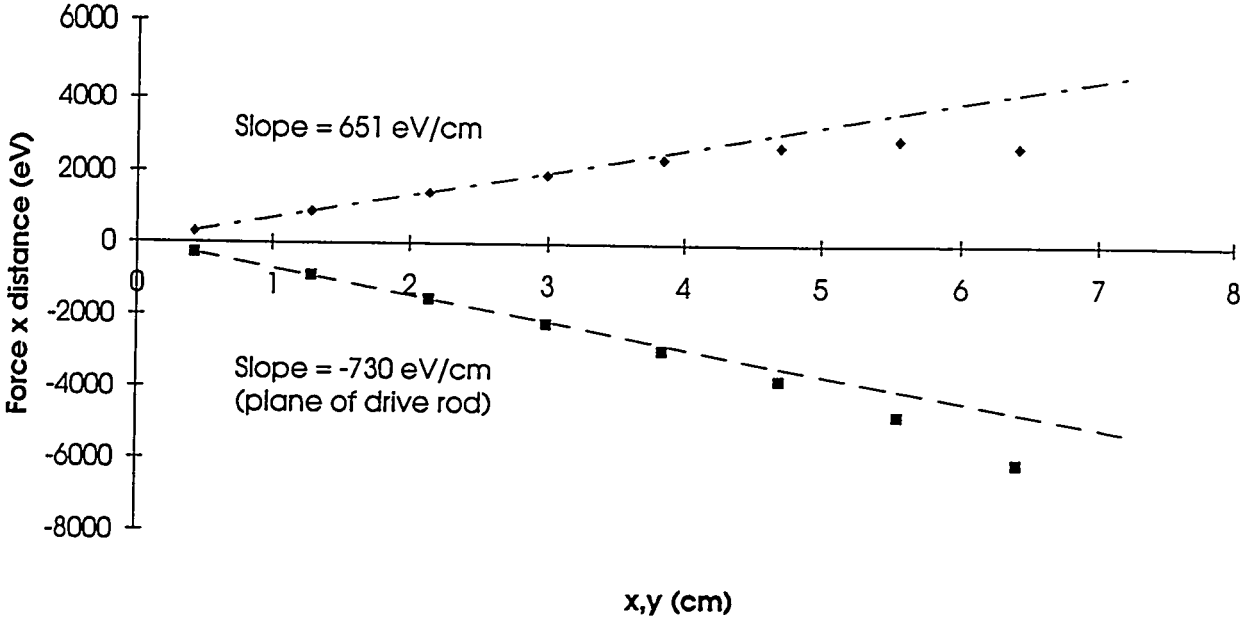

Figure 6. Radial variation of integrated transverse force vs. radius along x-axis (plane of drive-rods) and y-axis. The dashed lines are straight-line fits to the first three points. (Run L12).

A second set of calculations used the modified geometry in Fig. 3, where the ferrite was modeled as a region with a given μ, rather than as a perfect conductor. To get a base measurement, we first ran with $\mu = 1$ (i.e., the permeability of free space). This gave a quadrupole strength of 2.4 gauss, which is slightly higher than the 2.3 gauss obtained for the geometry in Fig. 2. We then ran with $\mu = 250$, the approximate low-frequency, low-signal value measured at LLNL (Ref. 4). This increased the quadrupole strength to 2.96 gauss, presumably due to magnetic field enhancement by the ferrite in the region of the drive rods.

2.1.3 Analytic Calculation

A simple analytic estimate of the quadrupole strength is obtained by considering the geometry in Fig. 7, consisting of a beam pipe, a radial line and two rods shorting the gap. In the limit of small pipe radius, $a/g \ll 1$, where a is the beam-pipe radius and g is the gap width, the quadrupole strength due to current in the rods is easily estimated from the Biot-Savart expression for a wire, giving

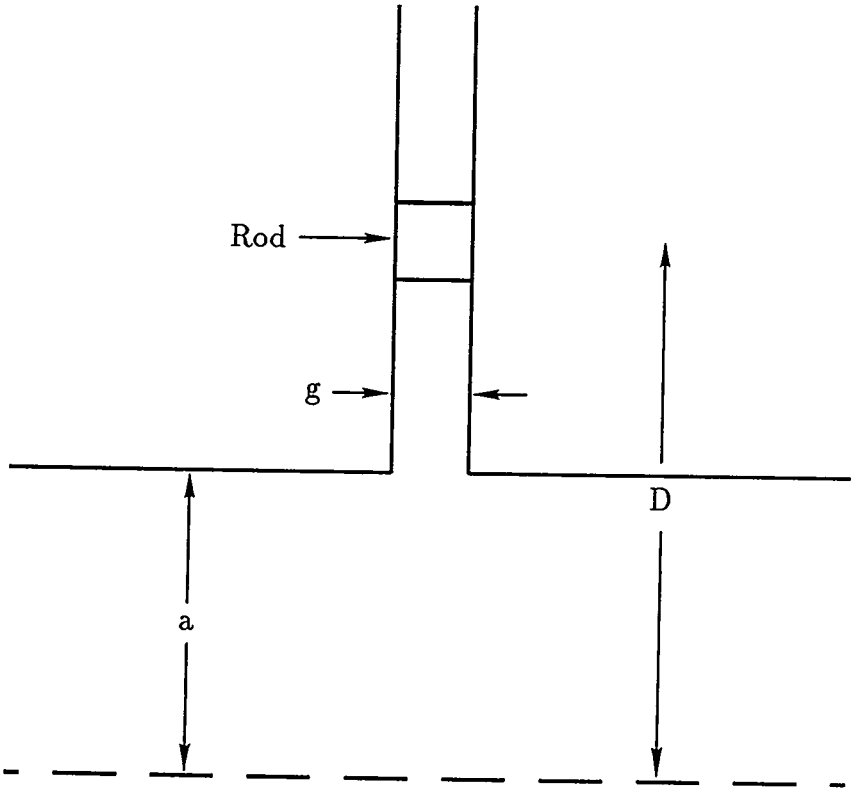

Figure 7. Simplified gap geometry used in Gluckstern-Cooper analytic calculation.

$$\int \left(\frac{\partial B_y}{\partial x}\right) dz = \frac{\mu_0 I_1 g}{\pi D^2} \quad \text{Tesla (MKS units)} \tag{3a}$$

or, equivalently,

$$\frac{Z_0 I_1\ (\text{A})}{300} \frac{g\ (\text{cm})}{\pi D^2\ (\text{cm})} \quad \text{gauss} \tag{3b}$$

where I_1 is the current carried by each rod, D is the radial position of the rods, and $Z_0 = 377\ \Omega$. For the DARHT cell parameters ($I_1 = 3000/2$ A, $g = 1.9$ cm, $D = 23.3$ cm) this gives 2.1 gauss (vs. 2.3 gauss from BTEC for the geometry in Fig. 2b).

Gluckstern and Cooper (Ref. 6) carried out an analytic calculation for this geometry for the opposite (small-gap) limit, which is more appropriate to the DARHT cell, and also considerably more complicated to treat. They obtain

$$\int \left(\frac{\partial B_y}{\partial x}\right) dz = \frac{Z_0 I_1}{300} \frac{2g}{\pi D^2 (1+Q_2)} \quad \text{gauss} \tag{4}$$

where Q_2 is a function of g/a (cf. Eq. 3b). For DARHT parameters, $Q_2 \approx 0.4$, and we obtain a value of 3 gauss from Eq. 4, vs. 2.3 gauss from BTEC. (References 3 and 6 appear to make an error in assuming that each rod carries the beam current rather than half the beam current, and thus obtain values a factor of 2 too high.)

To the extent that the sum of the leakage and beam currents is constant in time, the quadrupole force is also constant, and so can be corrected using a compensating static magnetic field. Variation of the sum of the currents will produce a time-varying quadrupole force.

2.1.4 BTEC vs. Analytic Results for Simple Geometry

As a check on the accuracy of BTEC, we did a simulation using the simplified geometry of Fig. 7, so that a direct comparison could be made with the analytic results of Ref. 6. A grid slice is shown in Fig. 8. The outer wall radius was made much larger than the rod radius, D, to minimize the effect of boundary conditions on the results. The transverse forces for a 3 kA driving current are shown in Fig. 9. The gradients in the x and y directions again differ by about 10%. Their average value gives a quadrupole strength of 7.8 gauss. Inserting the simulation dimensions into the analytic expression, Eq. 4, gives 7.6 gauss. This good agreement gives us confidence in the numerical results from BTEC for the more complicated geometries in Figs. 2 and 3.

2.2 Octopole Fields Due To Diagnostic Ports

To allow insertion of diagnostic targets into the beam line, a section of beam pipe with 4 ports was designed (Ref. 7). We have used a 3-D electromagnetic field solver to calculate the beam-induced fields in this structure. The main induced field is an octopole. We find that, at a radius of 6 cm, the magnitude of the force it produces is comparable to the net monopole self-field force of a 3 MV beam, i.e. it is a significant effect if the beam radius is large.

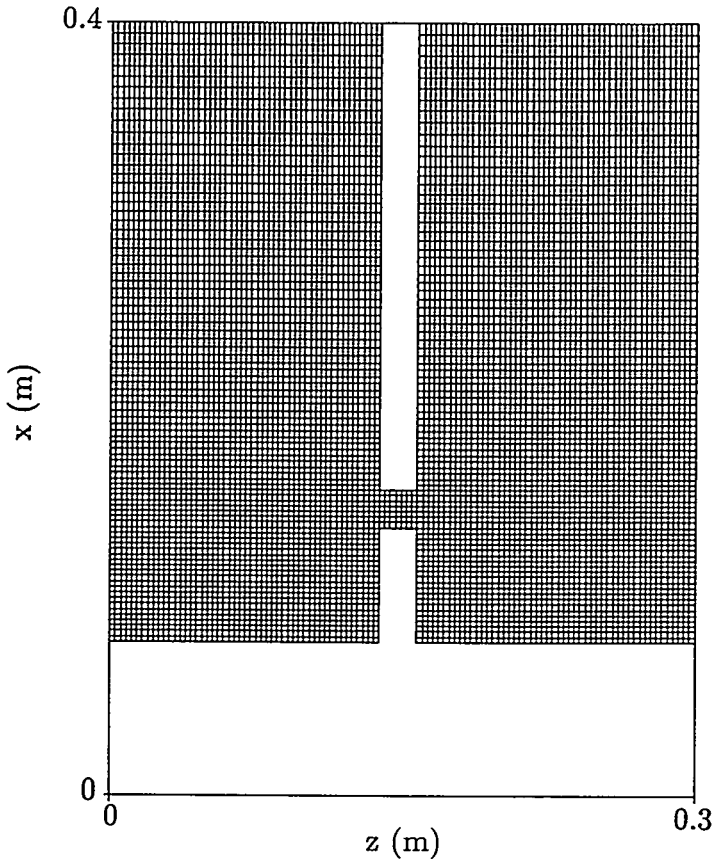

Figure 8. BTEC grid corresponding to Fig. 7, with dimensions $a = 8$ cm, $g = 2$ cm, and $D = 15$ cm.

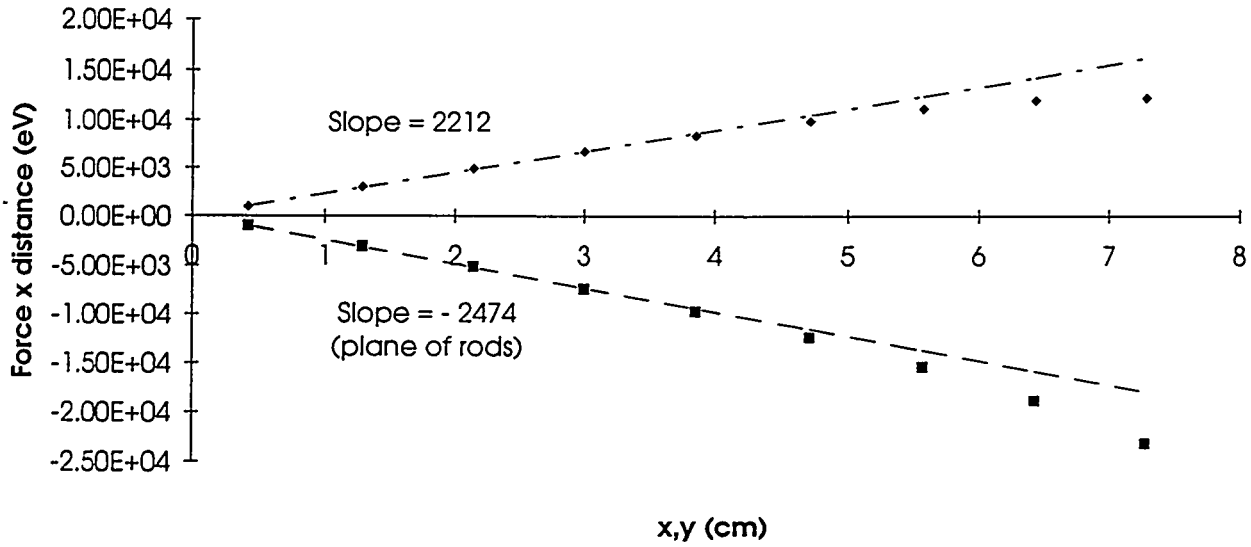

Figure 9. Radial variation of integrated transverse force along x and y axes for simplified geometry in Fig. 8. Dashed lines are straight-line fits to first four points. (Run L13).

2.2.1 Geometry

A sketch of the structure is shown in Fig. 10. Four symmetrically placed 3" by 8" holes are cut in a section of beam pipe. One of the four pipes providing access to the holes has a larger diameter than the other three. We neglect this in the calculation, making all four pipes identical. We use the 3-D gridded field solver BTEC (Ref. 1) to model the problem using dimensions as close to those of the actual device as allowed by the finite grid size. BTEC allows problems like this to be set up reasonably easily by hewing objects such as cylinders and planes out of a 3-D mesh. Some cross-sections of the grid are shown in Fig. 11. The axial length of the region modeled is 37.5 cm.

2.2.2 Field Calculation

The fields we are interested in are the zero-frequency (steady-state) fields induced by the beam in the perfectly conducting structure. The steady-state electric potential in the beam pipe satisfies Laplace's equation, viz.

$$\nabla^2\phi = 0 \tag{5}$$

Functions of the form

$$\phi(r,\theta) = \phi_0 r^n e^{in\theta} \tag{6}$$

satisfy Eq. 5. The periodicity of the holes in θ leads us to expect that the induced potential will have a large component of the form

$$\phi(r,\theta) = \phi_0 r^4 e^{i4\theta} \tag{7}$$

This potential has four periods around the circumference of the pipe, which can be thought of as arising from 8 regions of alternating positive and negative charge, i.e. an octopole. The corresponding electric field is

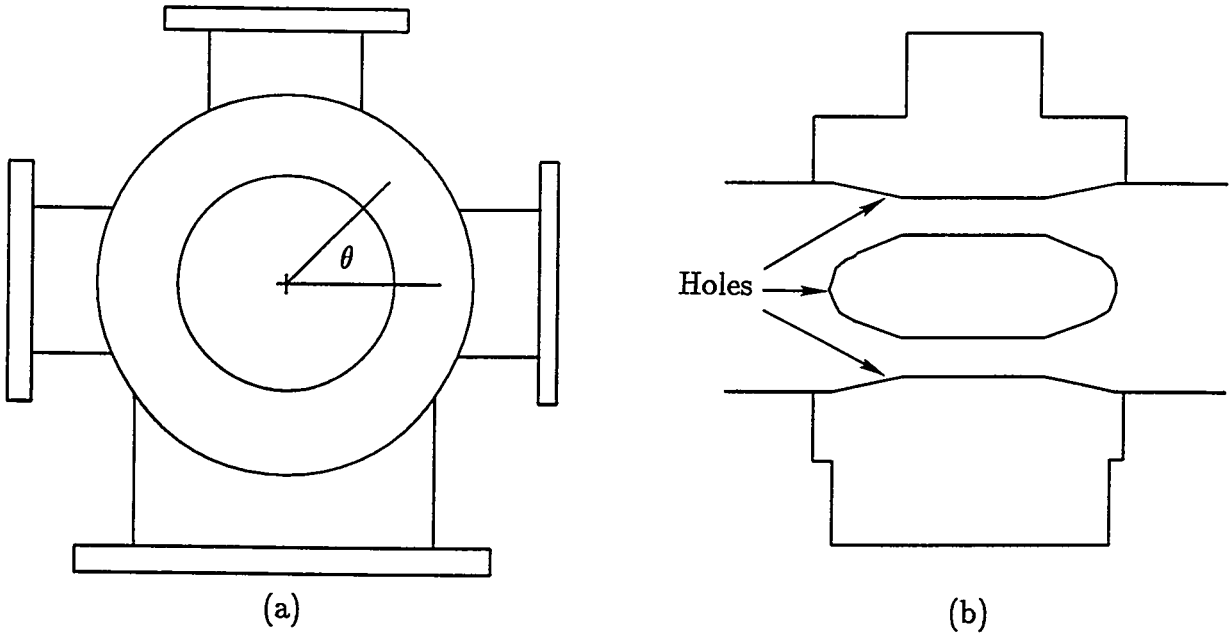

Figure 10. Sketch of 4-hole section of beam pipe looking (a) down the beam-line, and (b) transverse to the beam-line.

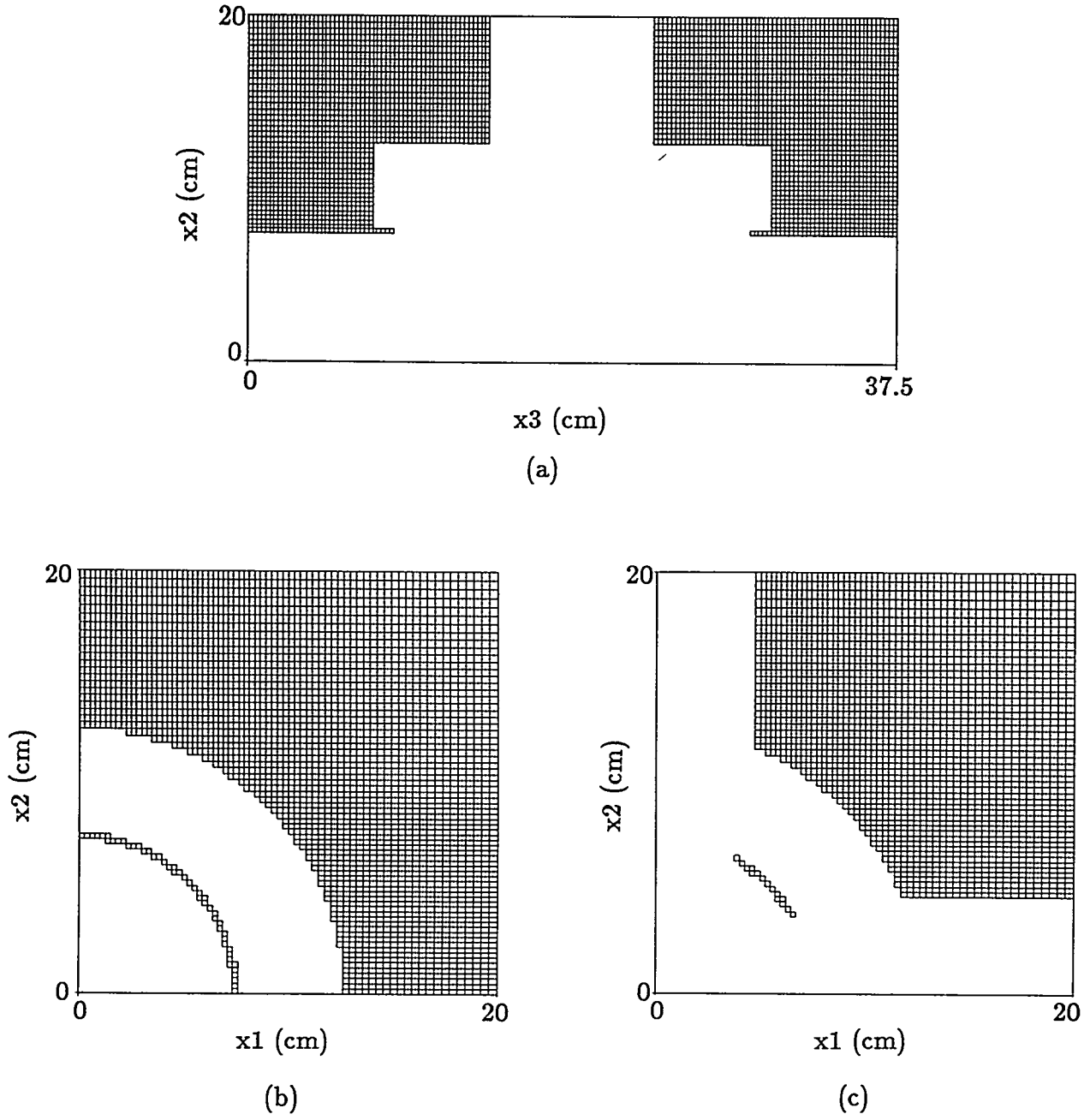

Figure 11. Sections of the 3-D BTEC grid used to compute the induced electric and magnetic fields. A slice through the axis of the beam line is shown in (a), a transverse slice with no holes is shown in (b), and a transverse slice through the center of the holes is shown in (c). Symmetry allows us to model just one quarter of the transverse space.

$$E_r(r,\theta) = -4\phi_0 r^3 e^{i4\theta} \tag{8}$$

Similar considerations apply to the magnetic field.

To obtain the induced fields using BTEC, we drive a current along the axis of the beam pipe and slowly ramp it in time to a value of 3 kA. "Slow" here means on a time scale long compared to the period of RF resonances of the beam pipe, which we do not wish to excite. For a pipe radius of 7.4 cm, the lowest RF resonances have a period of about 1 ns. The temporal profile of the drive current is shown in Fig. 12. We compute the effect of the holes on the beam by doing instantaneous integrals of the transverse Lorentz force along the beam pipe, viz.,

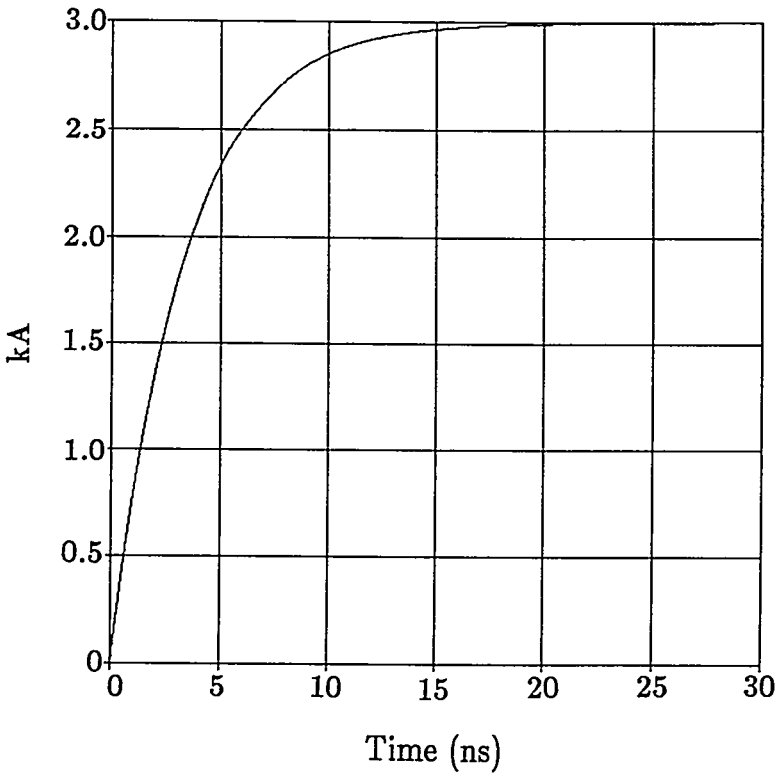

Figure 12. Temporal profile of axial current used to excite structure.

$$W(t) = e \int (\mathbf{E}_\perp - v_z \hat{z} \times \mathbf{B}_\perp)\, dz \tag{9}$$

where e is the electronic charge. To isolate the effect of the holes from the monopole self-fields of the beam, we use a current travelling at the velocity of light to excite the structure, and use $v_z = c$ in Eq. 9. In this situation, $W(t)$ is zero in a straight pipe, because the electric and magnetic forces cancel exactly. We compute $W(t)$ at a number of points along $\theta = 0$ and $\theta = 45°$ (see Fig. 10). As shown in Fig. 13, $W(t)$ oscillates about a mean value due to RF modes. We average over these oscillations to obtain the steady-state field value. The values are plotted versus radius in Fig. 14. We see that the numerical values are fitted reasonably well by the function

$$W_{\text{fit}}(r) = 120 r^3(\text{cm}) \text{ eV} \tag{10}$$

For comparison, the (analytically derived) integrated monopole force due to the self-fields of a 3 kA beam on a particle with energy γ over the 37.5 cm length of the simulation region is

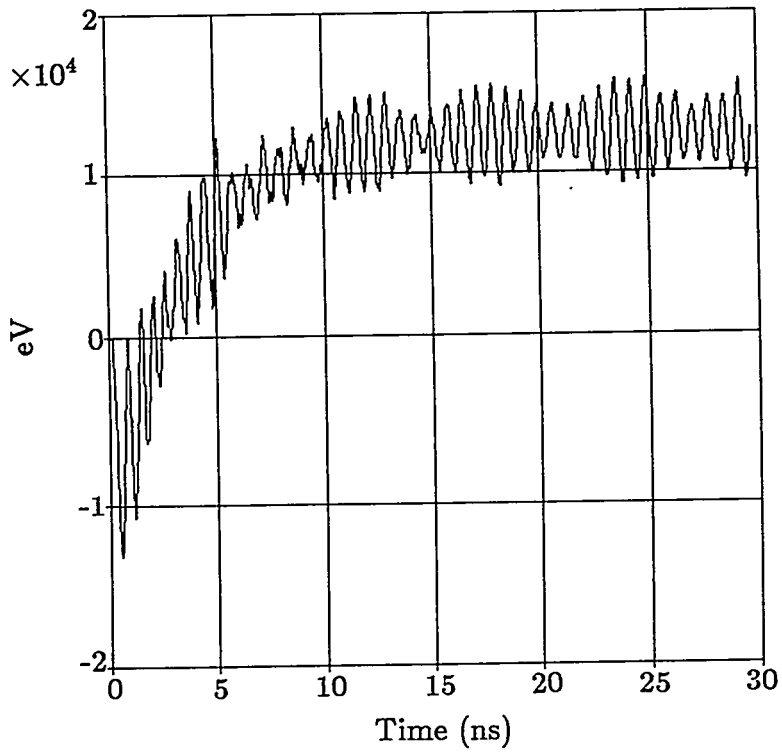

Figure 13. Temporal variation of integrated transverse force at $r = 4.834$ cm and $\theta = 0$.

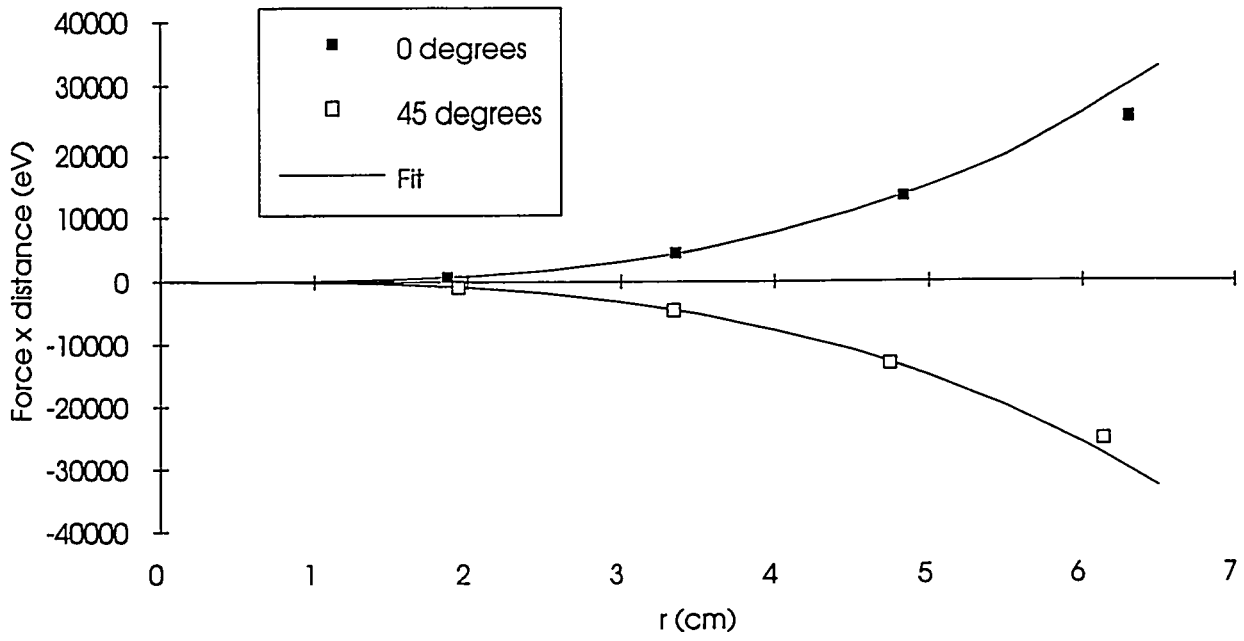

Figure 14. Radial variation of integrated transverse force vs. r for $\theta = 0, 45°$, overplotted by the function 120 r^3 (cm).

$$W_{\text{mono}}(r) = 6.76 \times 10^6 \Big/ \gamma^2 r \text{ (cm) eV} \tag{11}$$

(In Eq. 11, all the beam current is assumed to be inside the radius r.) Equating Eqs. 10 and 11, we find that for a 3 MV beam, the monopole and peak octopole forces are equal at a radius of about 5.9 cm. We verified this by redoing the calculation of $W(t)$ for a current travelling with $v_z = 0.989c$ (3 MV). The results are shown in Fig. 15, and we see that the predicted cancellation is occurring along $\theta = 45°$ near $r = 6$ cm. This comparison illustrates that the magnitude of the octopole field is non-negligible for large beam radii. The effect of the holes can be reduced by (a) reducing their size, (b) applying a compensating magnetic octopole or (c) ensuring that the beam has a small $\lesssim$3 cm) radius in this region.

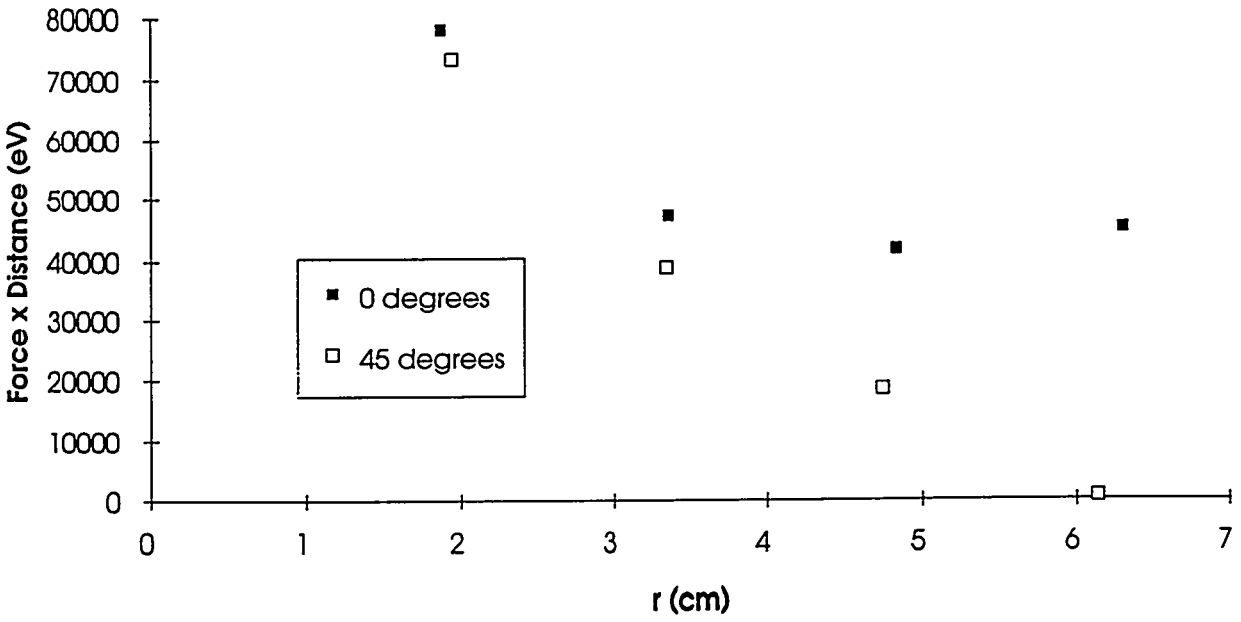

Figure 15. Integrated total (monopole + octopole) transverse force on a 3 MV particle showing that the monopole and octopole forces are approximately equal near $r = 6$ cm at $\theta = 45°$.

2.3 Recessed Cathode Geometry

The ITS has recently been testing cathodes where the emission surface is recessed from the surrounding electrode (See Fig. 16). The effect of the recess is to lower the axial electric field stress at the edge of the cathode and produce some radial electrostatic focusing in this region. Thus, the current density at the edge is reduced, and particles emitted at the edge are focused inward.

We calculated the effect of the cathode recess using PBGUNS (previously called SPEED) (Ref. 8). Recesses of 0, 2 and 3 mm were used. Results are shown in Fig. 17. The magnet settings for this calculation were (see Appendix B):

Bucking Coil:	-19.26 A
Focusing Coil:	170 A

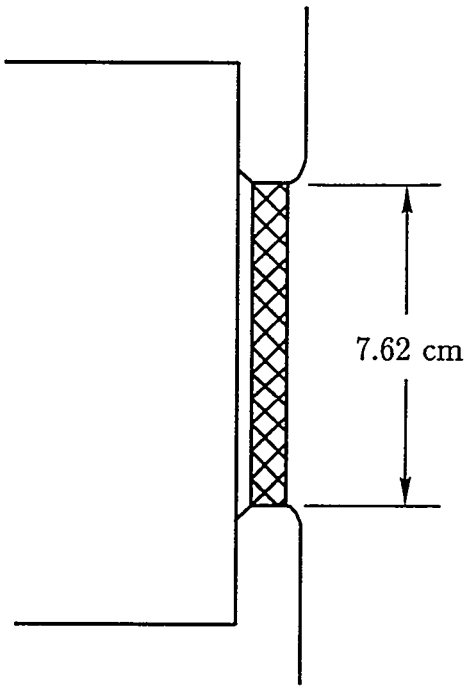

Figure 16. ITS cathode with recessed emission surface.

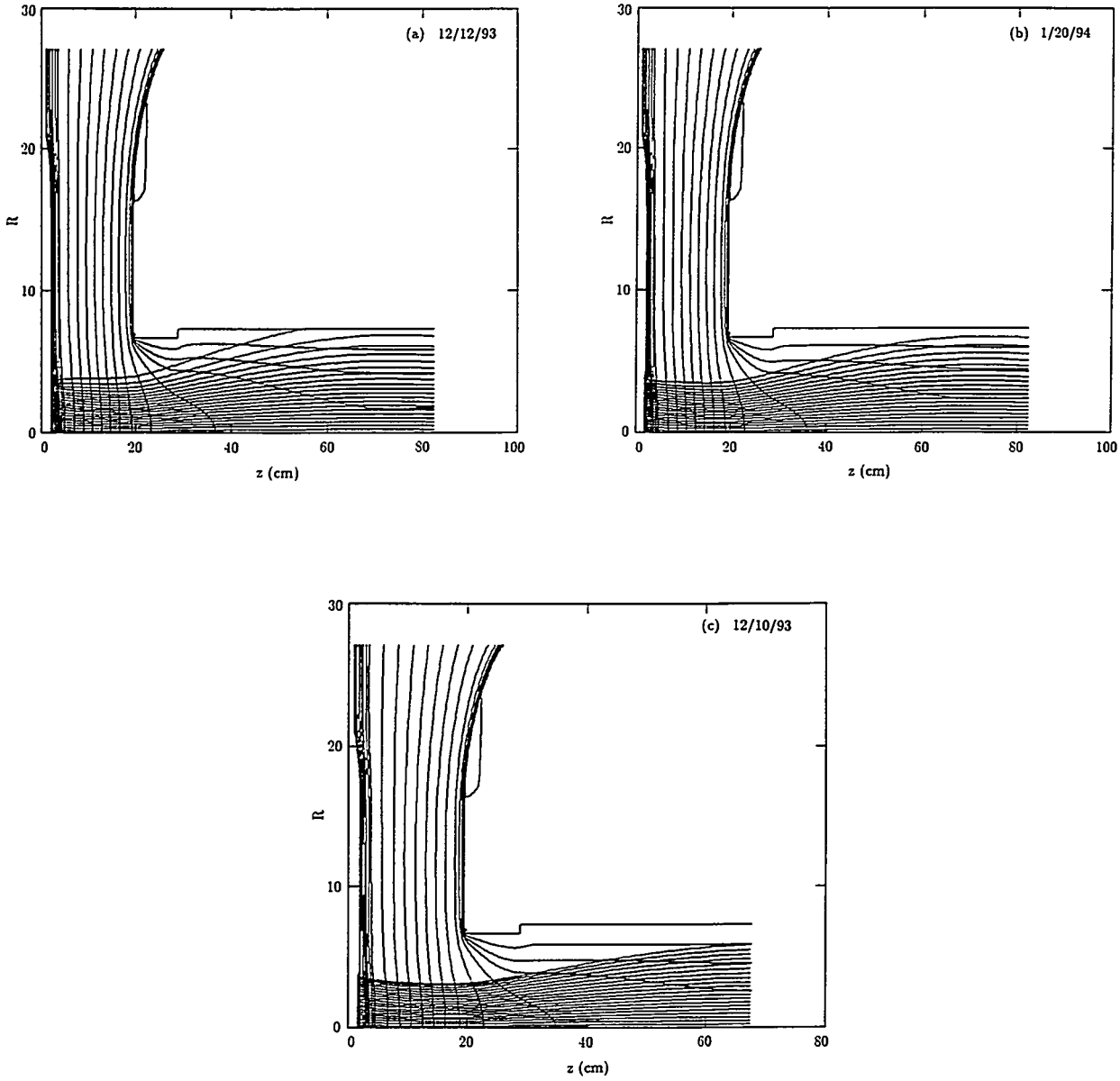

Figure 17. Trajectories and electric field equipotentials for cathode with recess of (a) 0, (b) 2, and (c) 3 mm.

For a voltage of 3.5 MV and an AK gap of 17.5 cm (the distance from the non-emitting cathode plane to the anode plane) the emitted and downstream currents were:

Recess (mm)	Emitted (kA)	Downstream (kA)
0	3.7	3.0
2	3.1	3.1
3	2.8	2.8

We see that the 2 and 3 mm recesses provide enough focusing to allow all the emitted current to get downstream. The recess also reduces the current density emitted off the edge of the cathode, as shown in Fig. 18.

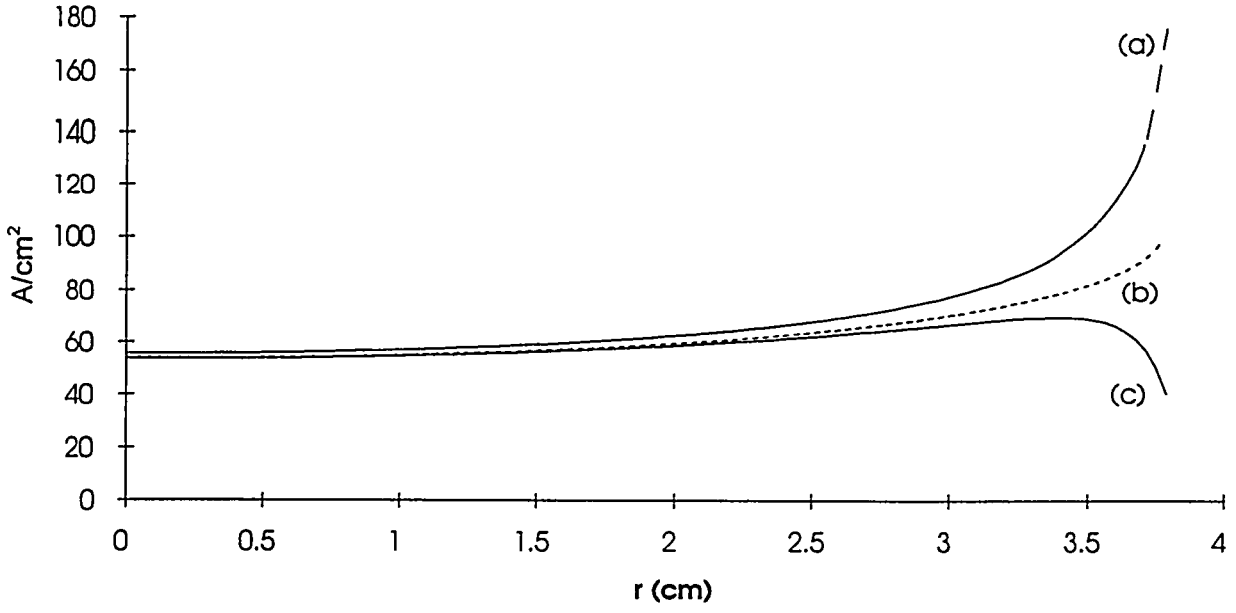

Figure 18. Current densities at the cathode surface for the three cases in Fig. 17, viz. recess of (a) 0, (b) 2 and (c) 3 mm.

In ITS experiments, a current of 3 kA was measured for the 2 mm recess, and essentially all of the current was transported to BPM-2, which is just downstream of the anode magnet. This contrasts with previous results with flush cathodes (Ref. 9, pp. 22, 45), where some

current was always lost between BPM-1 and BPM-2. In addition, for the flush cathode configuration in Ref. 9, the calculated emitted current was 3.0 kA vs. a measured value of 3.5 kA.

The improved agreement between experiment and calculation in the diode region will allow us to get more accurate initial conditions for downstream calculations using, e.g., LAMDA.

2.4 Comparison of LAMDA with BREAKUP

The LAMDA and BREAKUP codes were both used to model the Milestone 5 experiments for the DARHT review in June 1993 (see Ref. 10). The codes gave similar, but not identical, results. We subsequently ran some tests with the two codes in collaboration with Bernhard Kulke (LLNL), eliminating as many variables as possible. The accelerating gaps were removed, the coupling between the beam envelope and centroid was turned off in LAMDA, and wall forces were also turned off. Thus, we propagated the centroid of a constant voltage beam (3.1 MV) through the solenoidal magnetic field of the first seven cells. The beam was started with an initial sinusoidal deflection of amplitude 0.01 rads at the location of the tickler cavity. The frequency of the deflection was 740 MHz. The "gain" was then computed as follows. First, an FFT was performed on the x and y centroid data over the 60 ns flat-top of the pulse. A power integral was then performed over the frequency range 740 ± 75 MHz, giving X_{740}^2 and Y_{740}^2. The gain at the n^{th} BPM ($n = 5, 6$) was then defined by

$$g(n) = \frac{\sqrt{X_{740}^2(n) + Y_{740}^2(n)}}{\sqrt{X_{740}^2(3) + Y_{740}^2(3)}}$$

This procedure is the same as that used to measure beam breakup instability gain for Milestone 5. The gains at BPM's 5 and 6 are plotted as function of beam energy in Fig. 19. In order for the codes to agree the BREAKUP results have to be shifted to the right by 0.1 MV, i.e., LAMDA results for 3.1 MV agree with those for BREAKUP at 3.0 MV. The beam trajectory depends on the energy and the magnetic field only in the combination B/γ. Thus, the discrepancy could be due to a 3.3% difference in either the beam energies or in the magnetic field being used by the two codes. The code comparison has not been pursued since Dr. Kulke's retirement from LLNL.

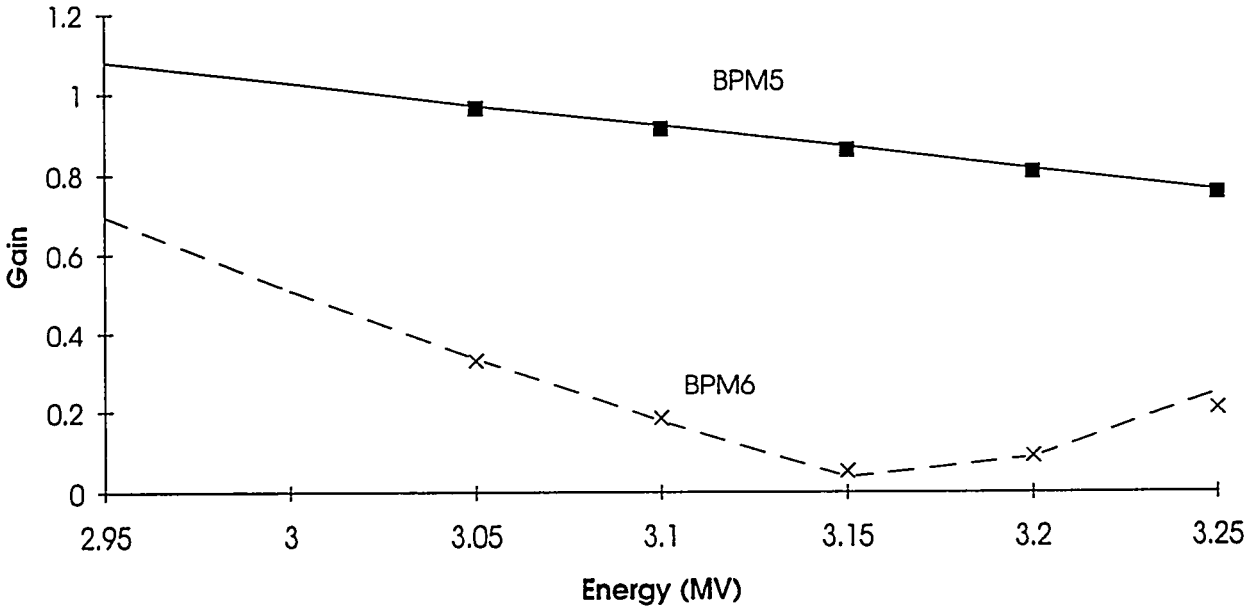

Figure 19. Comparison the LAMDA (solid line) with BREAKUP (symbols) showing gains measured at BPM 5 and 6 as a function of beam energy. *The LLNL results have been moved to the right by 0.1 MV.*

3.0 PHERMEX CALCULATIONS

3.1 Beam Radius vs. Magnet Strength

Beam extraction experiments were carried out on the PHERMEX thermionic flat cathode in preparation for doing beam transport experiments. The extraction experiments focused the beam onto a mask located 55.75 cm from the cathode electrode. The beamlets created by the mask then drifted 20.5 cm to a Bicron-422 scintillator. The beam radius at the mask was measured as a function of magnet strength. We used SPEED (Ref. 8) to model this experiment. The experiment used a cathode with a 0.15 cm indentation of the emission surface from the surrounding electrode. In the SPEED calculations the indentation was set to 0.25 cm, since a 0.25 cm $\times$ 0.25 cm mesh was used. This difference has little effect on the gross beam motion. Because of convergence problems, the simulation was carried out in two overlapping pieces. Emission was modeled out to 34 cm from the cathode electrode and trajectory and potential information was saved at 24 cm from the electrode (to eliminate end effects). A second simulation was then performed to take the rays from 24 cm to 76.25 cm, the location of the scintillator. Between the mask at 55.75 cm and the scintillator, the self-fields of the beam were turned off, since only a tiny amount of beam current gets through the mask in the experiment.

Plots of the downstream part of the two-part simulations for various magnetic field strengths are shown in Fig. 20. The magnet calibrations are given in Table 1. The measured calibrations are much closer to the calculated values than those previously reported (Ref. 11, p. 30).

The beam radius at the emittance mask as a function of magnet strength is shown in Fig. 21. Agreement between calculation and experiment is very good. As a result, we believe that the thermionic injector is well understood.

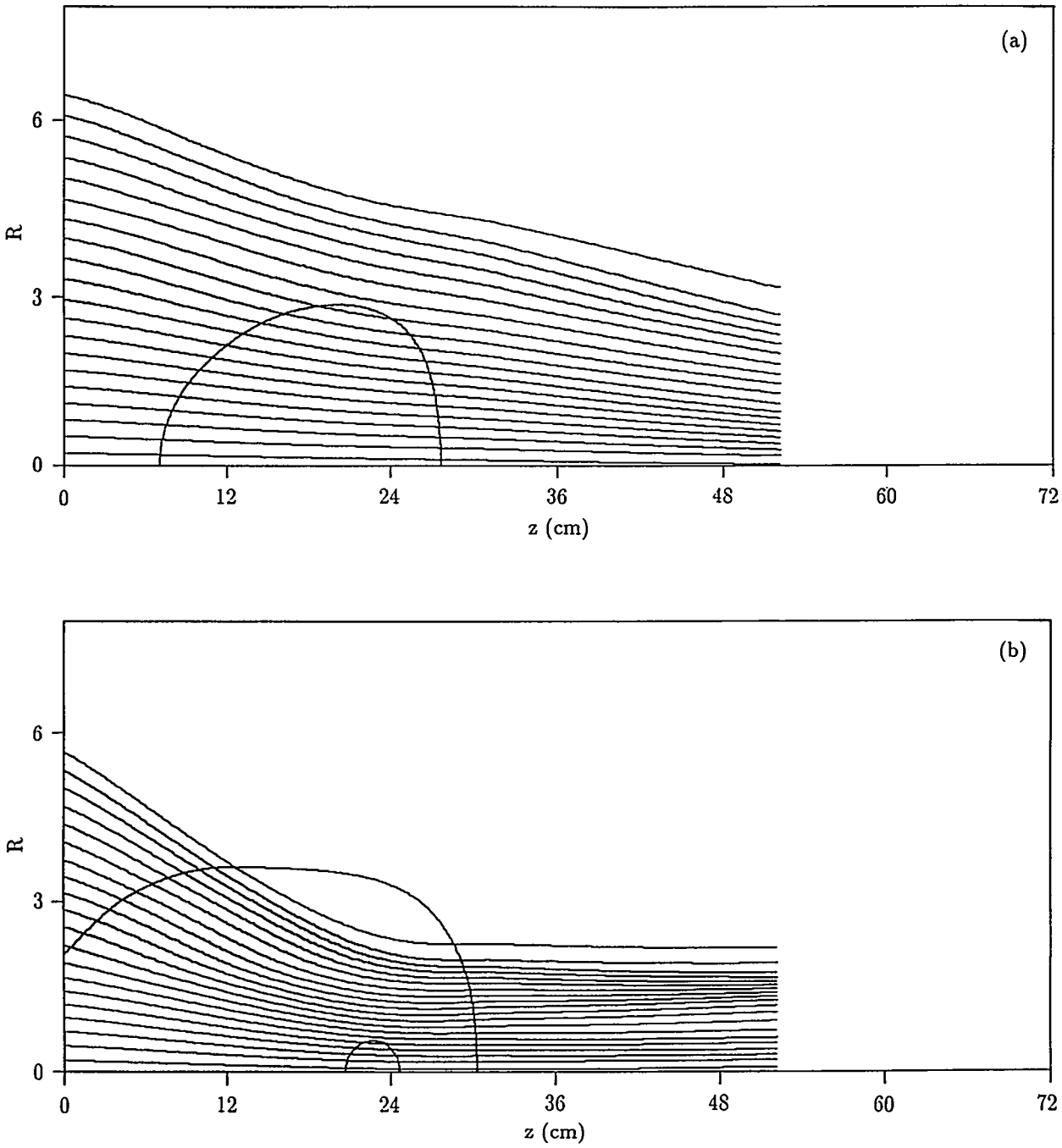

Figure 20. Downstream beam trajectory and equipotential plots for focus-coil currents of (a) 200 A, (b) 220 A, (c) 230 A and (d) 250 A. The emittance mask is at $z = 31.75$ cm. (The origin in these plots is at 24 cm from the cathode electrode.)

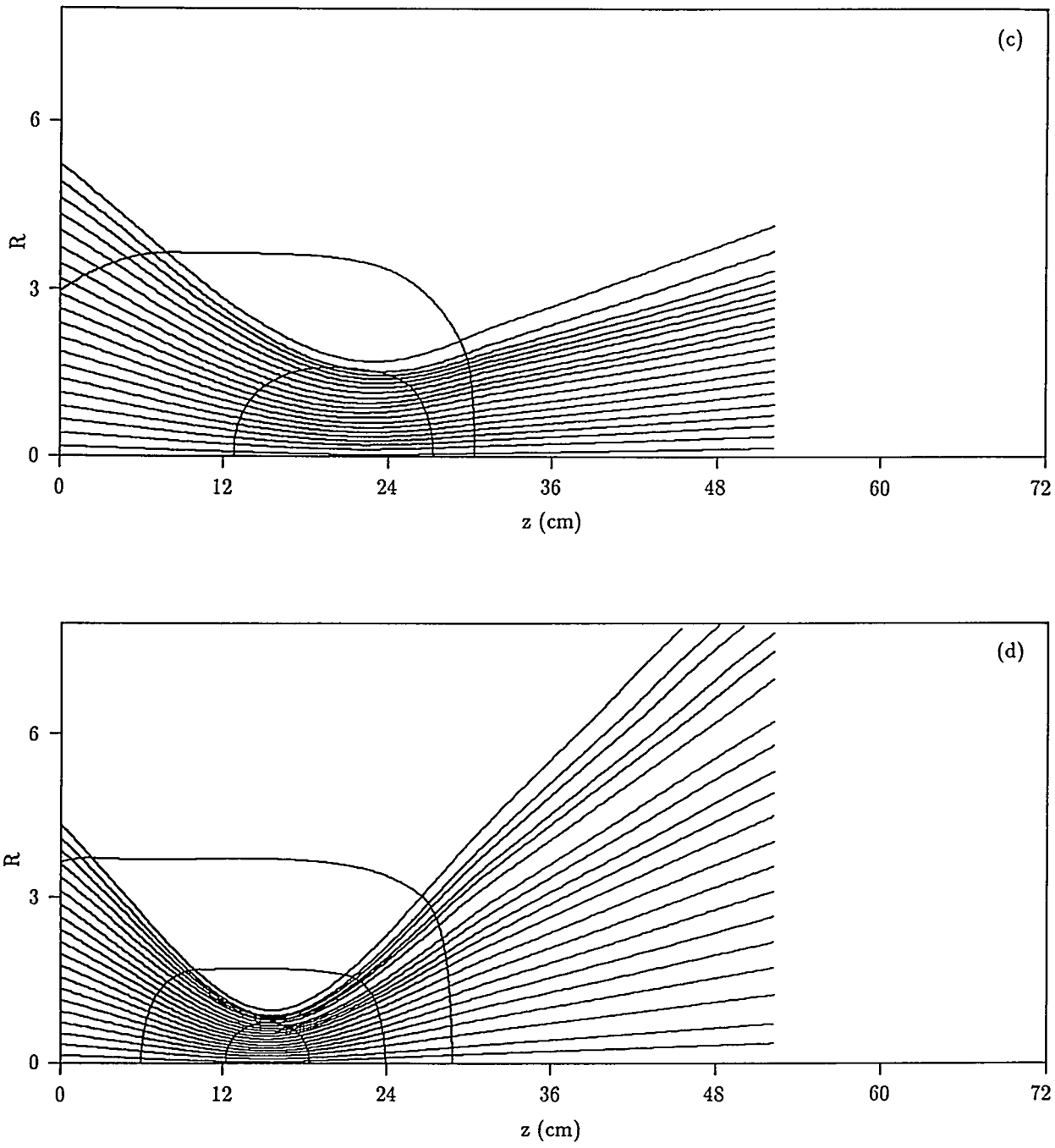

Figure 20. Continued. Downstream beam trajectory and equipotential plots for focus-coil currents of (a) 200 A, (b) 220 A, (c) 230 A and (d) 250 A. The emittance mask is at $z = 31.75$ cm. (The origin in these plots is at 24 cm from the cathode electrode.)

TABLE 1. PHERMEX injector magnet calibrations.

	Measured (gauss/Amp)	Calculated (BFIELD) (gauss/Amp)
Focus Coil:	3.25	3.236
Bucking Coil:	1.25	1.248
Trim Coil:	1.247	1.253

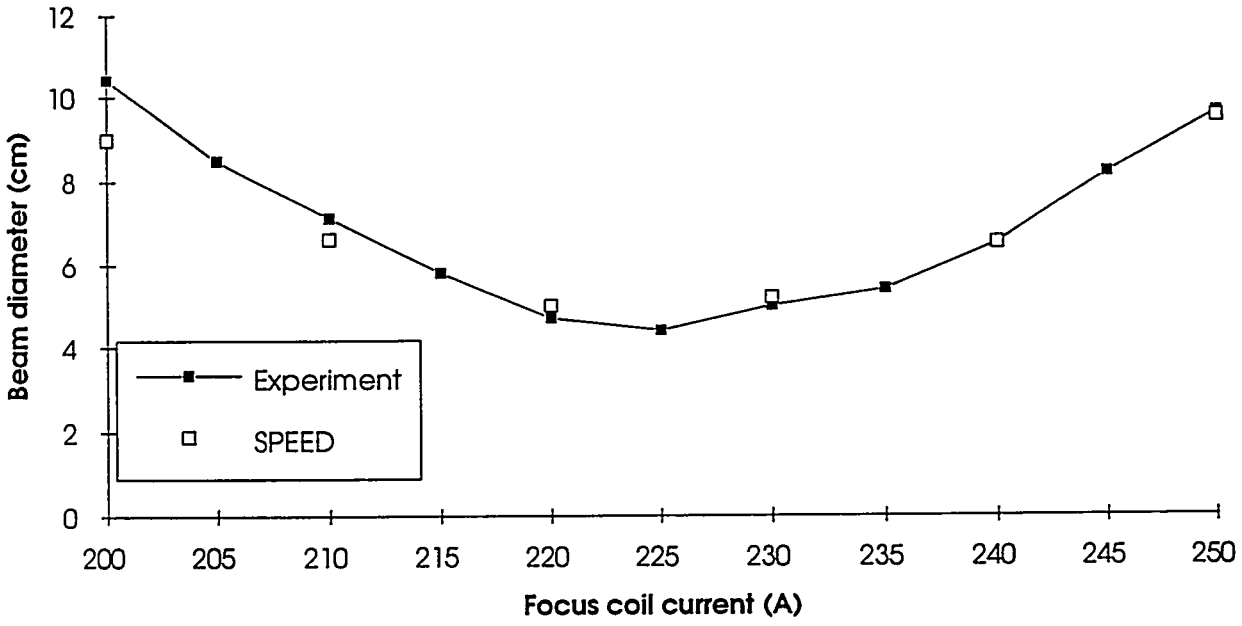

Figure 21. Beam diameter at emittance mask vs. focus coil current. Experimental data agrees well with SPEED calculations.

3.2 Emittance Reduction Using the Trim Coil

The trim coil in the PHERMEX flat-cathode injector allows modification of the radial profile of the magnetic field. The ISIS simulations carried out in designing the field coils (Ref. 12, p. 4) showed that the trim coil could significantly lower the downstream emittance of the beam. We reran these calculations using SPEED, both to confirm the ISIS results, and to obtain the $r - r'$ phase space of the beam. The calculation in Fig. 22 shows the trajectories and the emittance vs. z. The geometry, voltage and magnet settings are the same as those of the ISIS simulation in Ref. 12, p. 6. At 602 kV, SPEED gives an emitted current of 1.43 kA (vs. 1.46 kA from ISIS). The downstream emittance is somewhat higher than that obtained from ISIS. The $r - r'$ plot in Fig. 23(a) suggests that the trim coil setting is too high since the outer part of the beam is underfocused. Based on this, we lowered the trim-coil from -192 A to -136 A, and obtained a lower emittance, as shown in Fig. 24. The other magnets were adjusted to give the same net focusing strength as in Fig. 22. Comparing Fig. 23(a) and 23(b), we see that lowering the trim coil helps considerably to straighten out the phase-space, thereby lowering the emittance.

The differences between the SPEED and ISIS results may be due to the difference in numerical resolution ($\Delta z \times \Delta r = 0.5$ cm $\times$ 0.25 cm in ISIS vs. 0.25 cm $\times$ 0.25 cm in SPEED). In any case, the results suggest that in the experiment, one should vary the amplitude of the trim coil (keeping the net focusing strength fixed) in attempting to achieve an optimal setting.

At a voltage of 450 kV, the optimal magnet settings gave the results shown in Fig. 25. Note that at this lower voltage, it was necessary to *increase* the trim coil strength from the value at 602 kV to get the best results.

3.3 Optimization of Transport Magnet Settings

The beam extracted from the flat-cathode injector is transported through a solenoidal channel consisting of three separately adjustable coils. A sketch of the configuration is shown in Fig. 26. The original PHERMEX channel had two magnets, providing the two knobs needed to control the beam radius and convergence angle at the entrance to the α-cavity (see Ref. 13, p. 20).

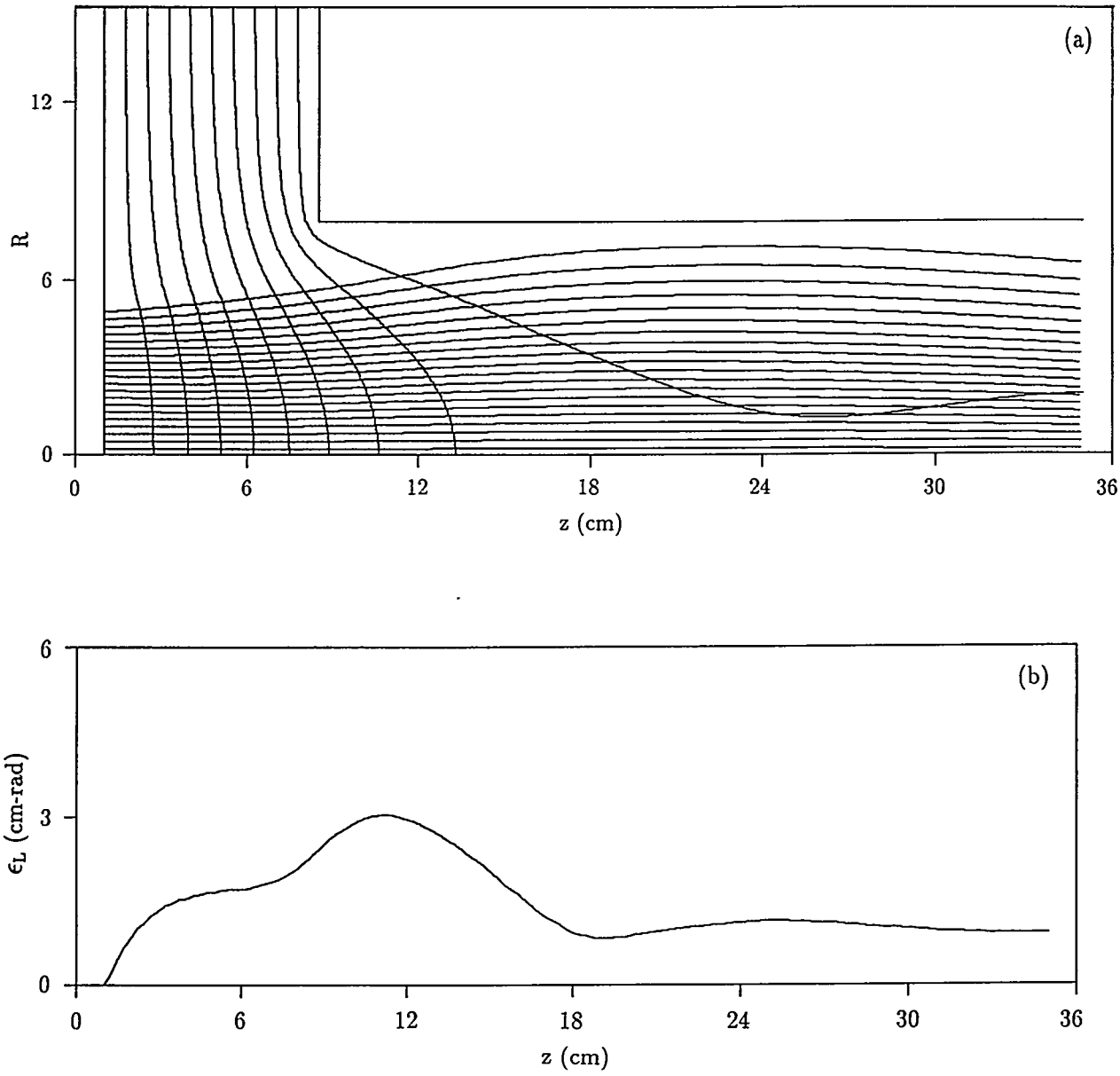

Figure 22. Flat cathode simulation at 602 kV showing (a) trajectories and (b) emittance vs. z. Magnet settings are: focus coil = 310 A, bucking coil = -490 A, trim coil = -192 A. Phase-space at $z = 31$ is shown in Fig. 23(a).

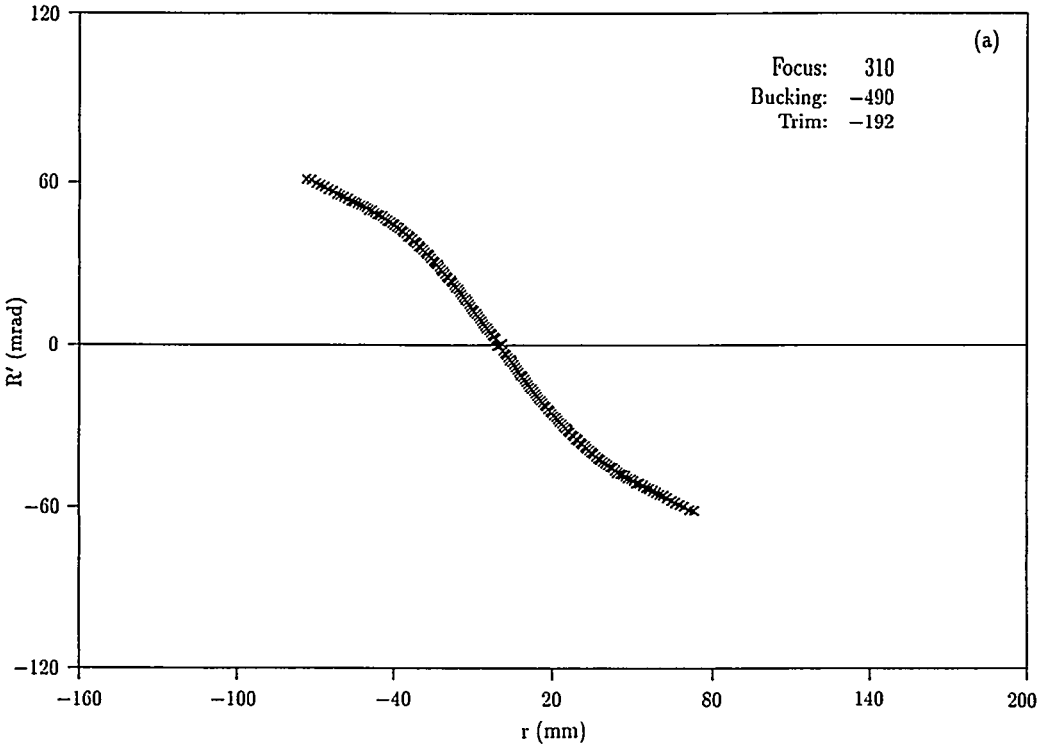

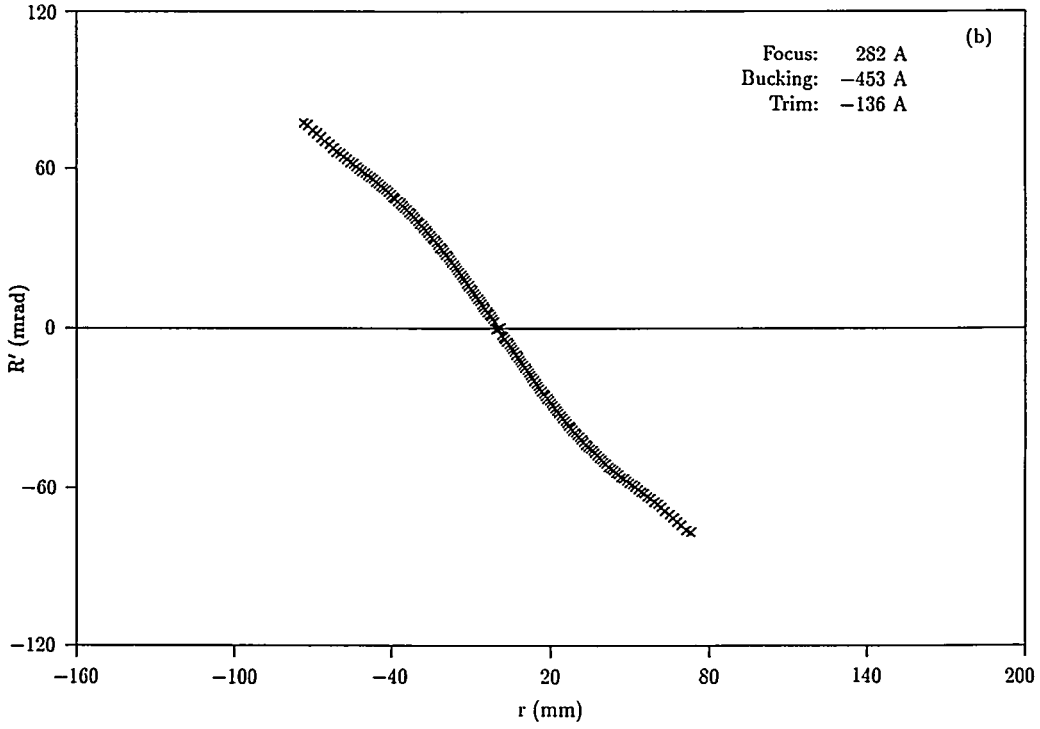

Figure 23. $r - r'$ phase space plots 29 cm from cathode surface for two different magnet settings. The net focusing strength is the same for the two cases. (Runs 17, 17A).

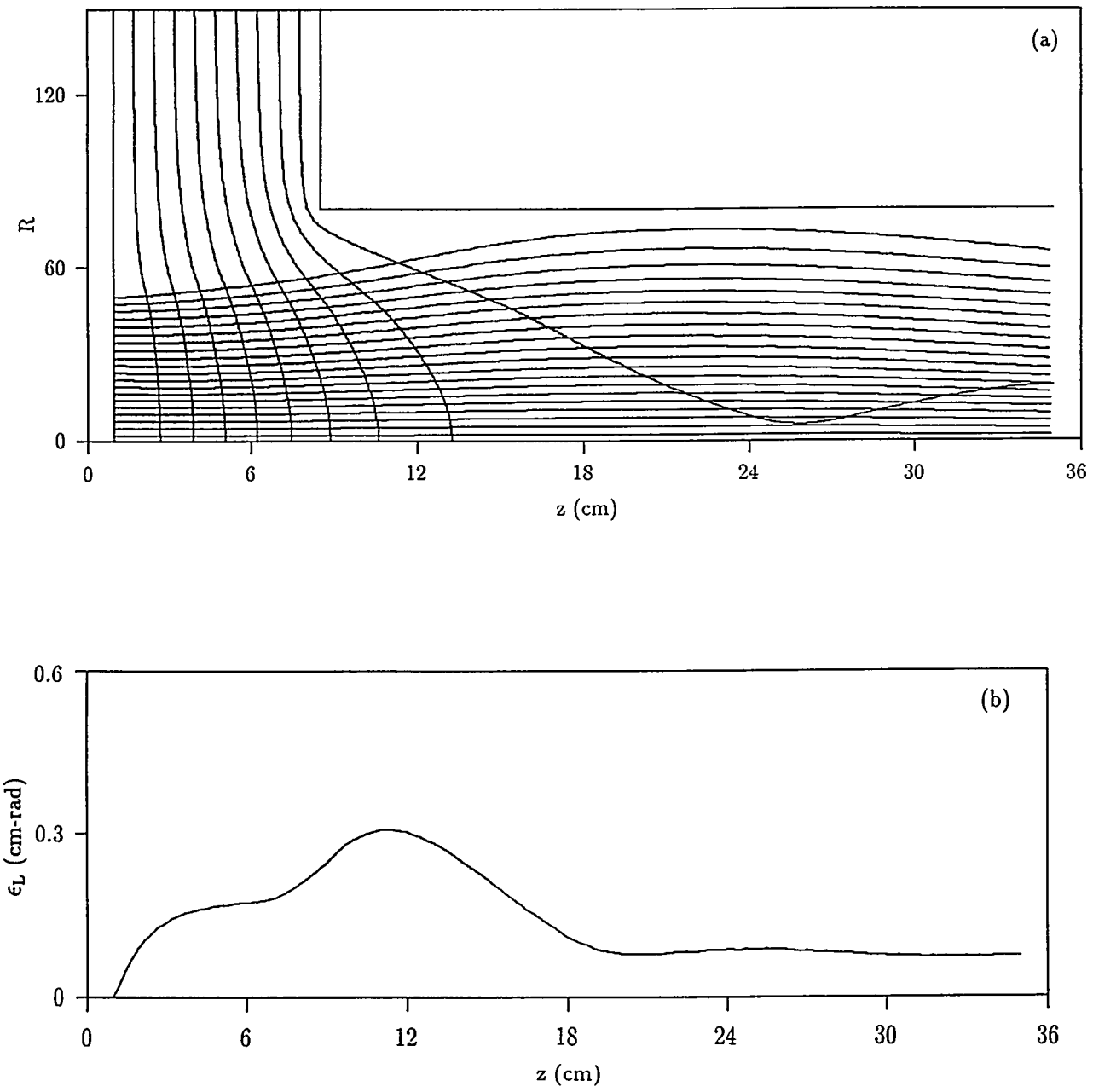

Figure 24. Flat cathode simulation at 602 kV showing (a) trajectories and (b) emittance vs. z. Magnet settings are: focus coil = 282 A, bucking coil = -453 A, trim coil = -136 A. Phase-space at $z = 31$ is shown in Fig. 23(b).

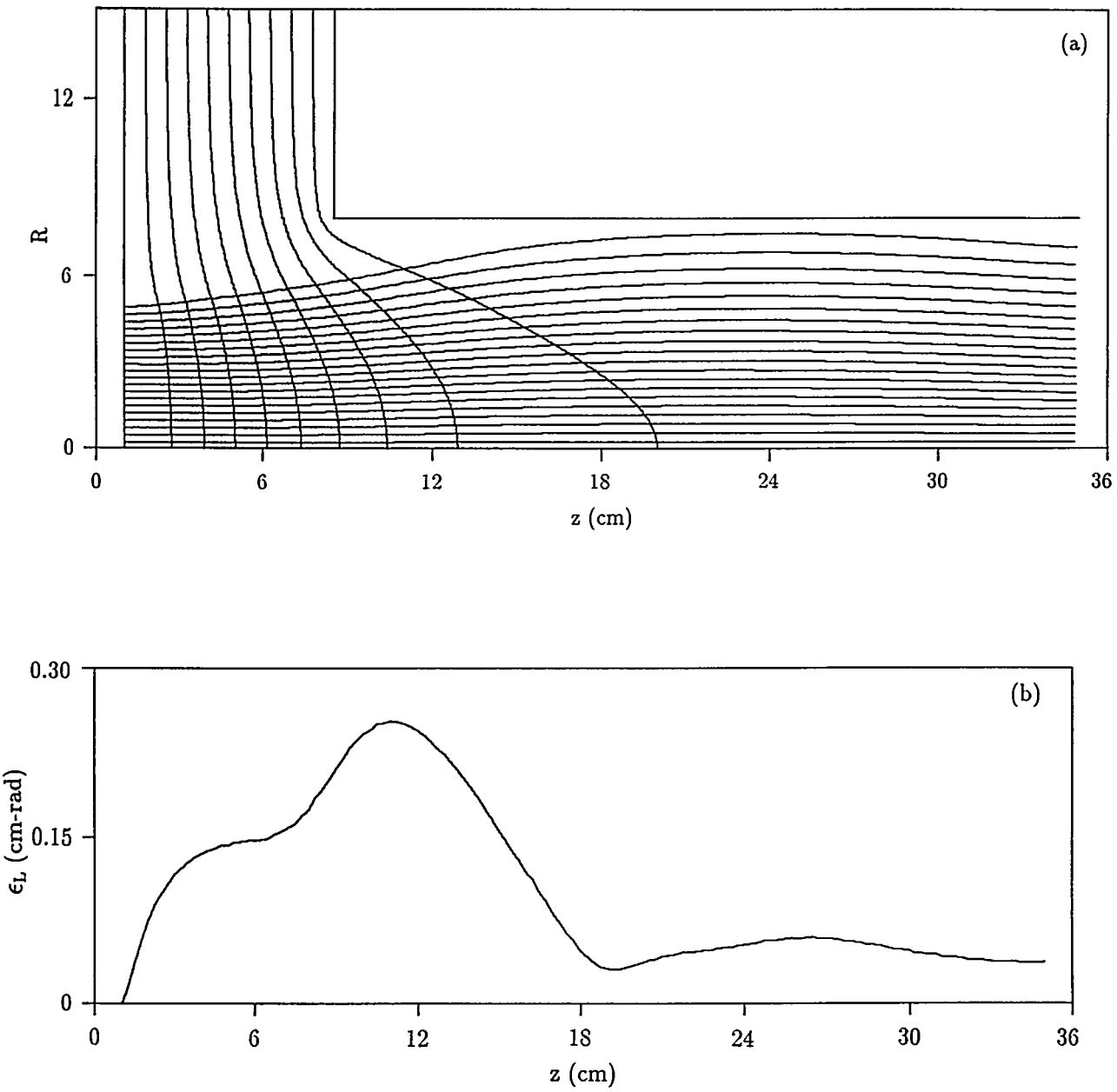

Figure 25. Flat cathode simulation at 450 kV showing (a) trajectories and (b) emittance vs. z. Magnet settings are: focus coil = 254 A, bucking coil = -402 A, trim coil = -157 A.

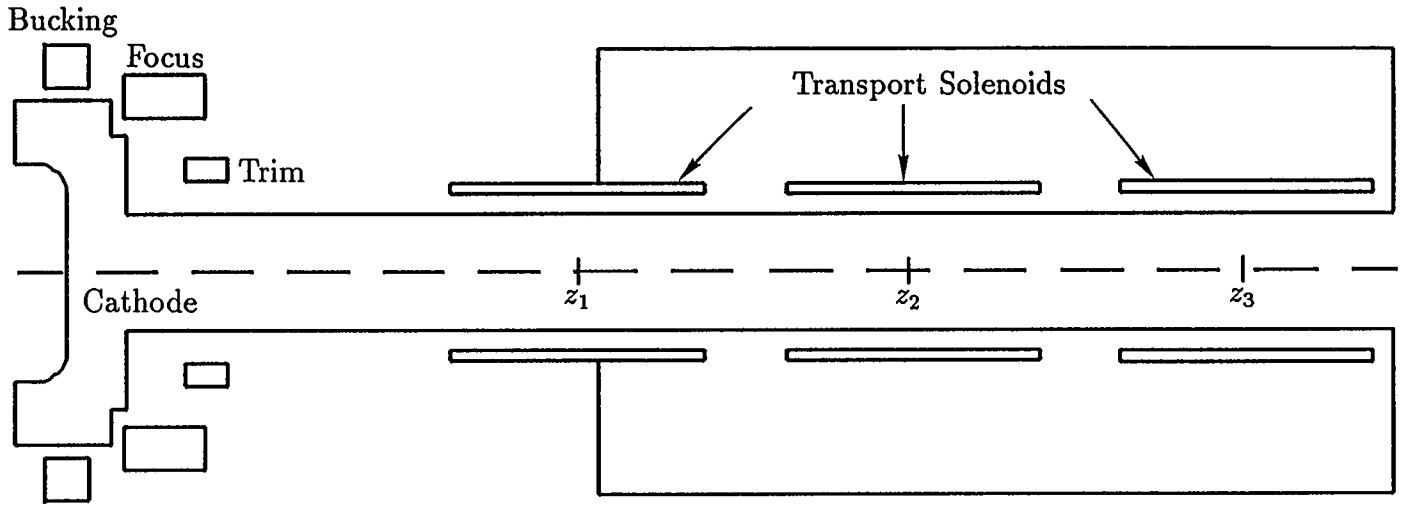

Figure 26. Schematic of PHERMEX transport experiment. The centers of the transport solenoids, measured from the cathode, are at $z_1 = 66.65$ cm, $z_2 = 109.26$ cm and $z_3 = 151.8$ cm. The emittance mask was at $z = 178$ cm.

In order to reduce the tedium of varying the magnet settings by hand, we wrote an automatic optimization routine. This involves defining a function (known as the "cost function") which one wishes to minimize. The function we used was

$$F(c_1, c_2, c_3) = \left(\frac{R - R_0}{R}\right)^2 + 10\,(R' - R_0')^2 \tag{12}$$

where c_1, c_2, c_3 are the coil currents in the three magnets, and R_0, R_0' are the desired beam radius and convergence angle at the entrance to the α cavity (or at any other location). The factor of 10 appearing in Eq. 12 is arbitrary: it determines the relative weighting of the radius and slope. Values of $F(c_1, c_2, c_3)$ are calculated using an envelope code. A standard nonlinear optimization procedure is then applied to iteratively compute the values of c_1, c_2, c_3 which minimize F to some tolerance. ($F = 0$ means that the desired radius and slope have been achieved.) We tried both simulated annealing and Powell minimization (Ref. 14). Simulated annealing is a very general optimization algorithm which is best suited to problems where F is a non-smooth function of its arguments. We found the Powell procedure to be more efficient in our case, where F is a smooth function. Results showing initial and optimized settings are given in Fig. 27, where the desired radius and slope were $R_0 = 6$ cm, $R_0' = 0$, respectively. The initial conditions for the beam envelope in Fig. 27 were obtained from an IVORY simulation of the AK gap region.

Using these settings, we carried out an IVORY simulation of the diode and transport section, which is shown in Fig. 28.

The optimization procedure was repeated for a lower voltage of 477 kV. An IVORY simulation using the resulting magnet setting is shown in Fig. 29.

3.4 Comparison with Transport Experiments

A series of transport experiments was carried out in the fall of 1993 using a thermionic cathode. We ran IVORY simulations to compare with some of the measurements. The magnet settings are given in Table 2.

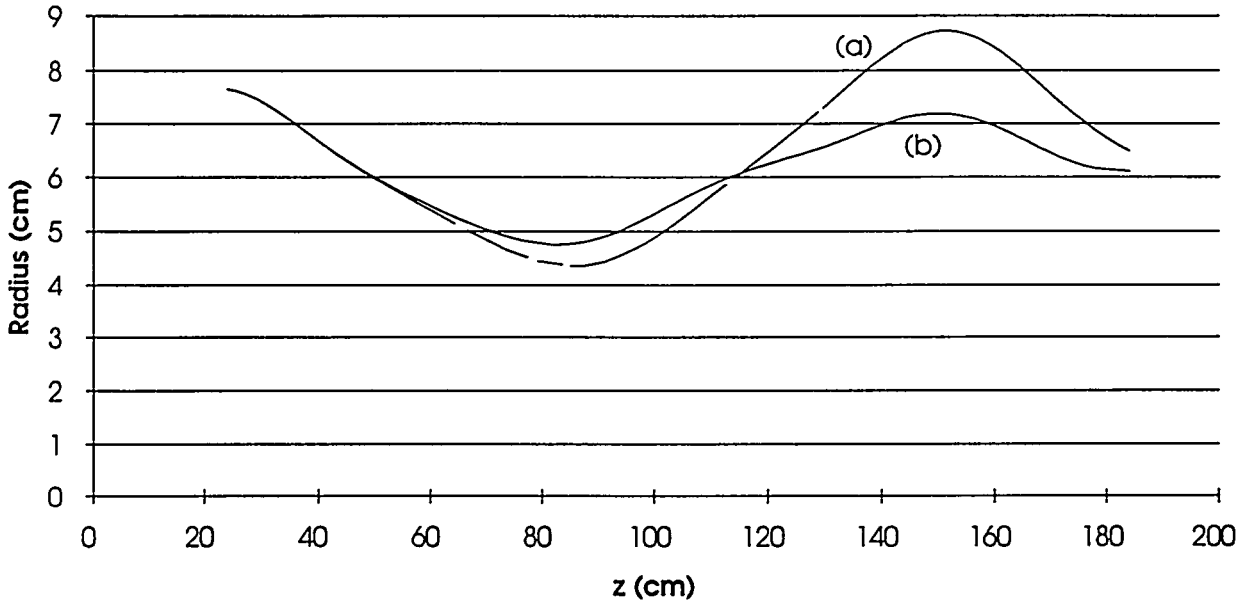

Magnet settings:

	Initial	Optimized
Solenoid 1	54	48
2	51	62
3	74	69

Figure 27. Beam envelope for (a) initial and (b) optimized transport magnet settings for PHERMEX injector. ($I_b = 1.37$ kA, $V_b = 0.596$ kV, $a = 7.65$ cm, $a' = -0.01$, $\epsilon_L = 0.05$ cm-rad, $R_{\text{wall}} = 8$ cm, $z_{\text{start}} = 24$ cm, $D = 160$ cm. Initial conditions obtained from /phermex/ivory/7.)

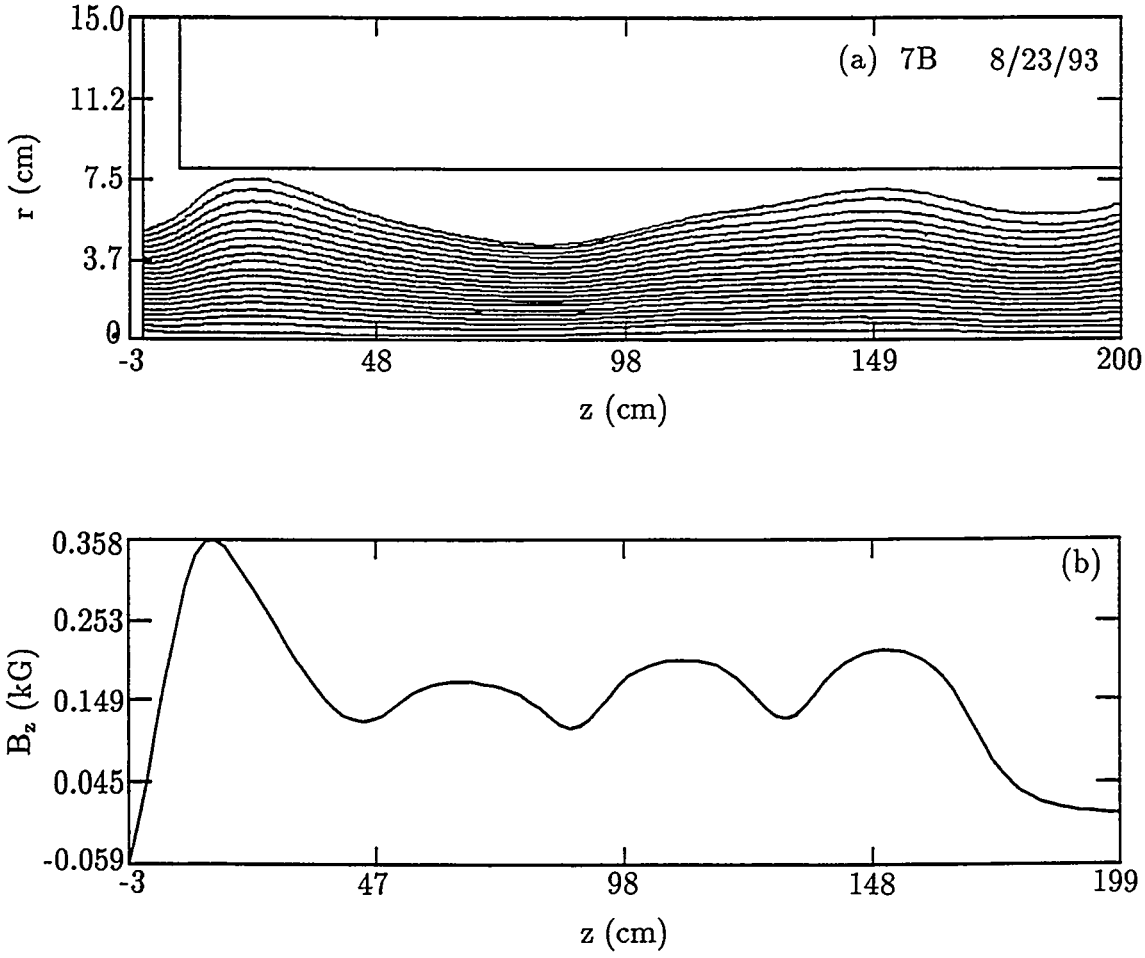

Diode magnet settings (Amps):

Focus		267
Bucking		-430
Trim		-129
Transport Solenoid	1	48
	2	62
	3	69

Figure 28. IVORY simulation of PHERMEX flat cathode and transport channel, using optimized magnet settings from Fig. 27, showing (a) particle trajectories and (b) axial magnetic field. The α-cavity wall is at $z = 182.9$ cm in this plot. ($V = 0.596$ MV, $I = 1.37$ kA, (/phermex/ivory/7b.)

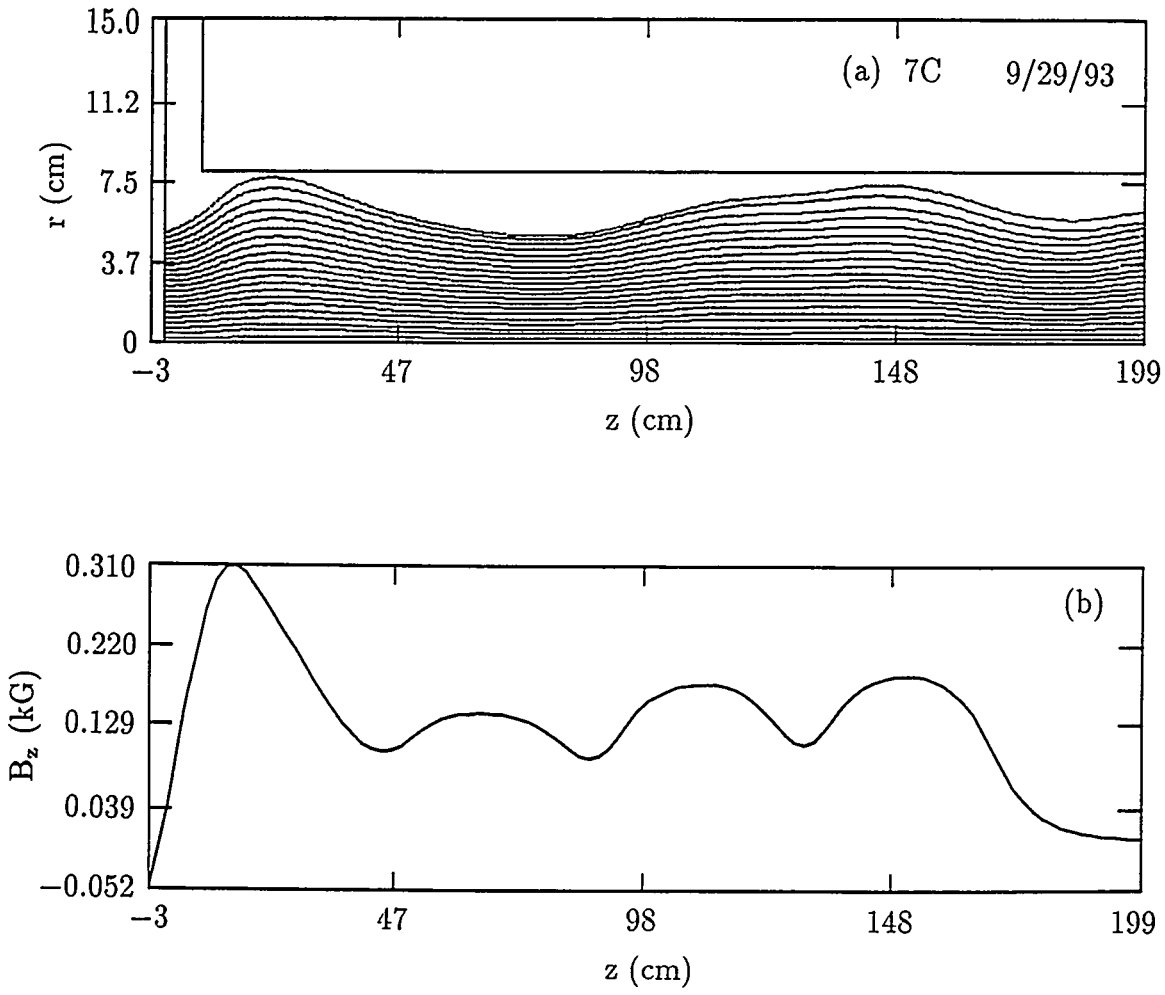

Magnet settings:

Focus	233
Bucking	-373
Trim	-112
Solenoid 1	41
2	54
3	59

Figure 29. IVORY simulation of PHERMEX flat cathode and transport channel using optimized magnet settings for 477 kV, showing (a) particle trajectories and (b) axial magnetic field. The α-cavity wall is at $z = 182.9$ cm in this plot. ($I = 1$ kA, (/phermex/ivory/7c.).

TABLE 2. Magnet settings used in thermionic cathode transport experiments. (All magnet settings are in Amperes.)

Beam Voltage (kV)	530	540
Magnets:		
Focus	258	260
Bucking	-447	-445
Trim	-90	-110
Solenoid 1	65	75
2	75	80
3	80	80

The IVORY simulations used a flush cathode because resolving the 0.15 cm cathode inset is impractical in a long transport simulation. This results in an overestimate of the emitted current. The behavior of the beam envelope is not very sensitive to this, however. The results are shown in Fig. 30. In the experiment, emittance mask data were taken at 178 cm from the cathode surface. These data gave beam radii at 3.6 cm and 3.3 cm at 530 and 540 kV, respectively. The simulations give beam radii of 3.5 cm (at 530 kV) and 4 cm (at 540 kV). The simulation results in Fig. 30 indicate that the transport solenoid currents could be reduced to get a smoother beam envelope, like those in Figs. 28 and 29.

3.5 Effect of Temperature, Bucking Coil on Transport

The velvet cathode has a significantly higher effective temperature than the thermionic cathode. The IVORY simulation in Fig. 31 is a rerun of the simulation in Fig. 29 using an effective cathode temperature of 200 eV (instead of the zero temperature in Fig. 29). We see that the temperature causes some current loss (40 A) to the wall, but otherwise has a little effect on the beam transport.

During the velvet cathode experiments, it was observed that reducing the bucking coil strength resulted in increased current transport. We believe that this is the result of the

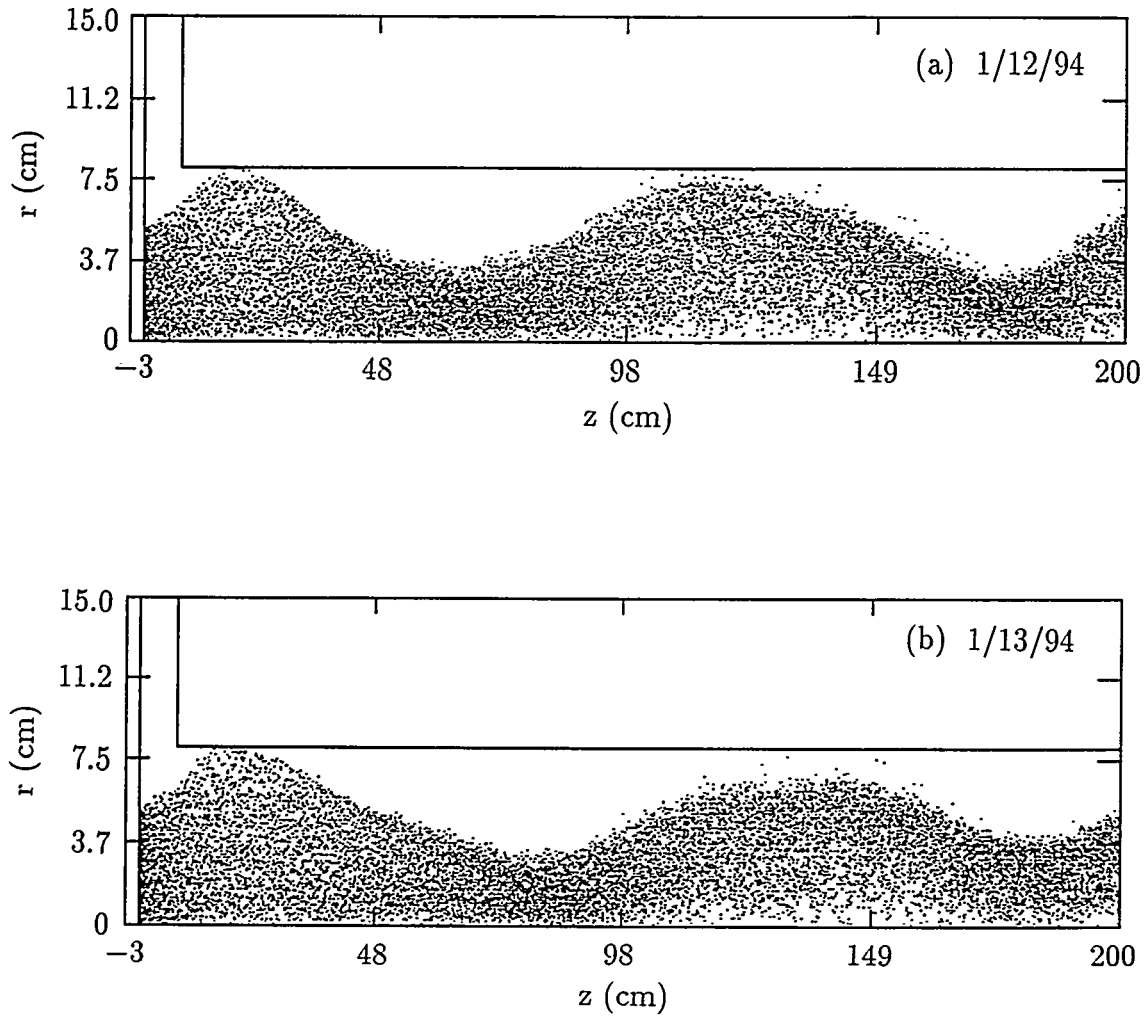

Figure 30. IVORY simulations of PHERMEX transport at (a) 530 kV and (b) 540 kV using the experimental magnet settings given in Table 2.

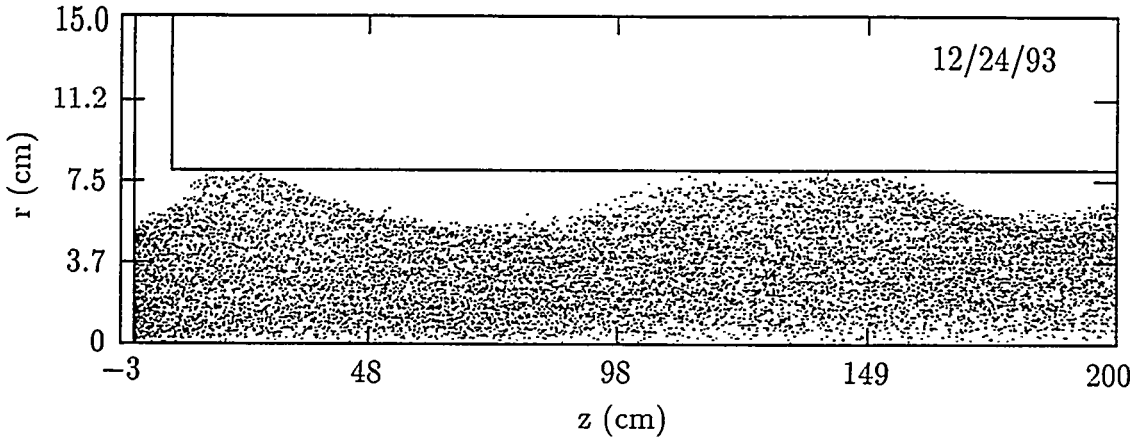

Figure 31. Beam envelope for 477 kV with 200 eV cathode temperature. Beam voltage, current and applied magnetic field are the same as those in Fig. 29. Current loss to wall is 40 A out of 1 kA.

increased net focusing strength, and not due to, e.g., the field on the cathode. Due to the small AK gap in the PHERMEX geometry (unlike the ITS geometry), the bucking coil has a strong effect on the net focusing strength of the injector magnets.

4.0 CODE DEVELOPMENT

4.1 IDL Postprocessor for LAMDA

The LAMDA code is currently run primarily on the ICN Cray machines. The main obstacle to moving the code to the ITS DECstations has been the lack of CGS-like graphics on these machines. CGS graphics are used by the VIEW postprocessor for LAMDA. To remedy this, we have written an IDL version of VIEW, described in the following. This description will be inserted into the next revision of the LAMDA user's manual.

In addition to the convenience of a graphical user interface, the IDL version is considerably faster than the current Fortran version since it reads all the data into memory once instead of reading from disk each time a plot is selected. The latter made VIEW excruciatingly slow on the Macintosh because of the Mac's poor I/O performance.

VIEW Postprocessor

VIEW reads the PLOT.xxx output file generated by LAMDA, and generates a graphical display of the data. There are two versions of the VIEW postprocessor. One is a portable Fortran code and the other is a GUI (graphical user interface) application written in the IDL language.

Fortran Version

The Fortran version uses a menu-driven interface similar to LINC and is described in Sec. 5.0 of the user's manual (Ref. 15).

IDL Version

The IDL version of VIEW requires an installed copy of IDL Version 3.1 or later (Ref. 16) (IDL runs on many platforms, including DECstations, IBM PC's and Macintoshes). When IDL is running, compile VIEW (if necessary) and start it by typing

```
IDL> .run view
% Compiled module: READ_DATA
  etc.

IDL> view
```

The screen shown in Fig. 32 appears. The top half of the display shows a list of plot labels (initially filled with "No Plot" labels since no file has been opened yet). The bottom half of the display is a graphics window. The top of the display has three "buttons", labeled "Done", "File", and "Tools", which have the following effects when clicked:

"Done": Quits VIEW and closes all associated windows

"File": Drops a menu from which one may open data files or obtain Postscript output for the currently displayed plot

"Tools": Currently used only for debugging purposes

To look at data, click on "File" and choose "Open LAMDA data file ..." from the menu. This brings up standard file-choosing boxes. VIEW reads the selected file and displays the plot labels it finds. A particular plot can be displayed by clicking on its label, or by scrolling to it with the arrow keys (see Fig. 33).

The graphical window initially has a button on top labeled "Raw Data", indicating that the data displayed is what is in the LAMDA data file. Clicking on this button brings down a menu with "Raw Data", "Windowed Data", and "FFT" selections, which have the following effects:

"Raw Data": Reverts to the data in the LAMDA data file

"Windowed Data": Brings up a box which allows one to specify the x and y plotting ranges manually (see Fig. 34). When the ranges are specified, clicking the "OK" button displays the windowed data.

"FFT": Brings up the windowing box (Fig. 34) to specify ranges for an FFT of the data. When "OK" is clicked, the FFT is displayed (see description in

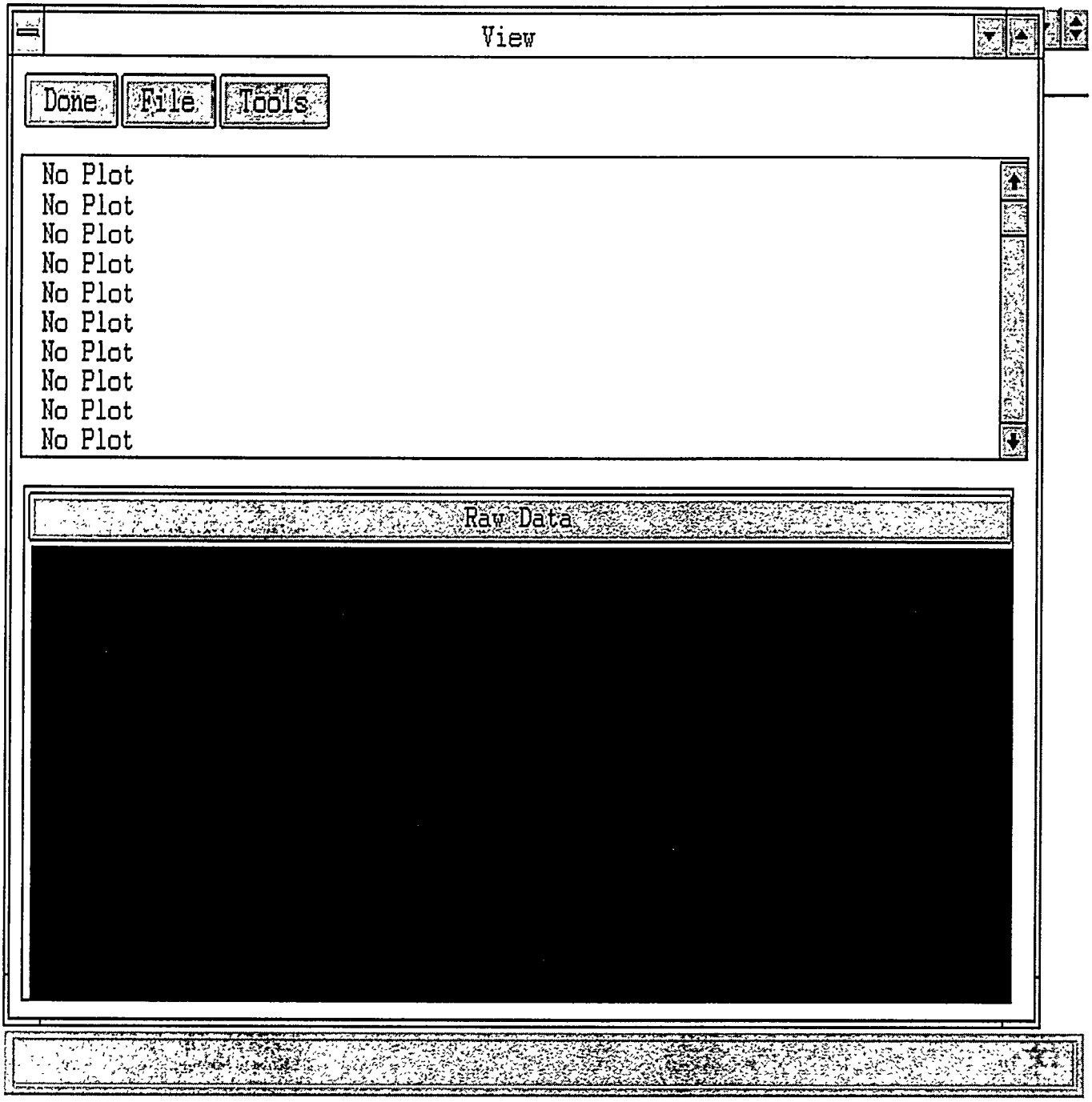

Figure 32. Initial VIEW display consists of IDL "widgets": buttons, ("Done", "File", "Tools", "Raw Data") scrollable list of plot labels, and graphics window.

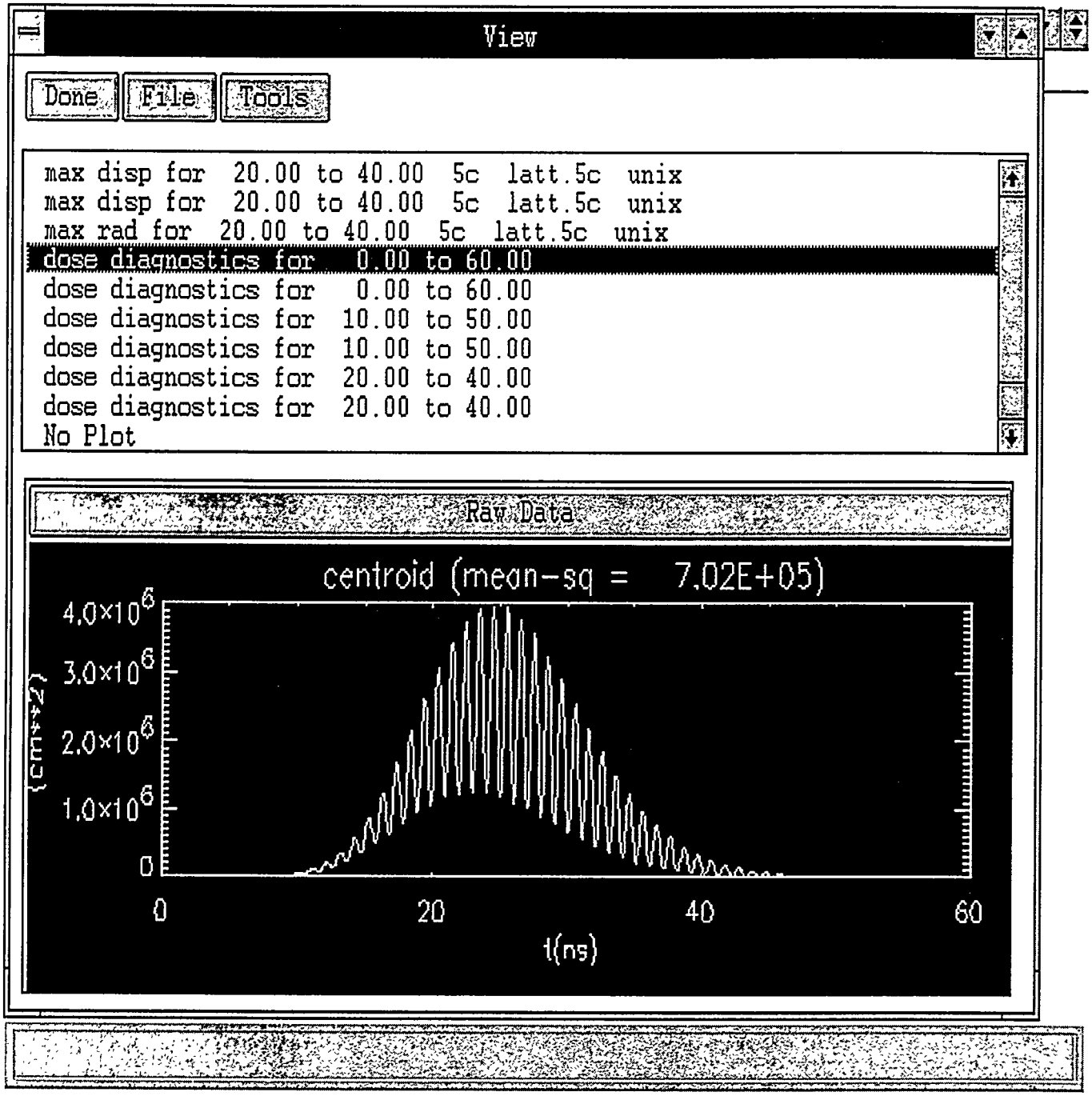

Figure 33. VIEW display showing list of plot labels on top and the selected plot on the bottom.

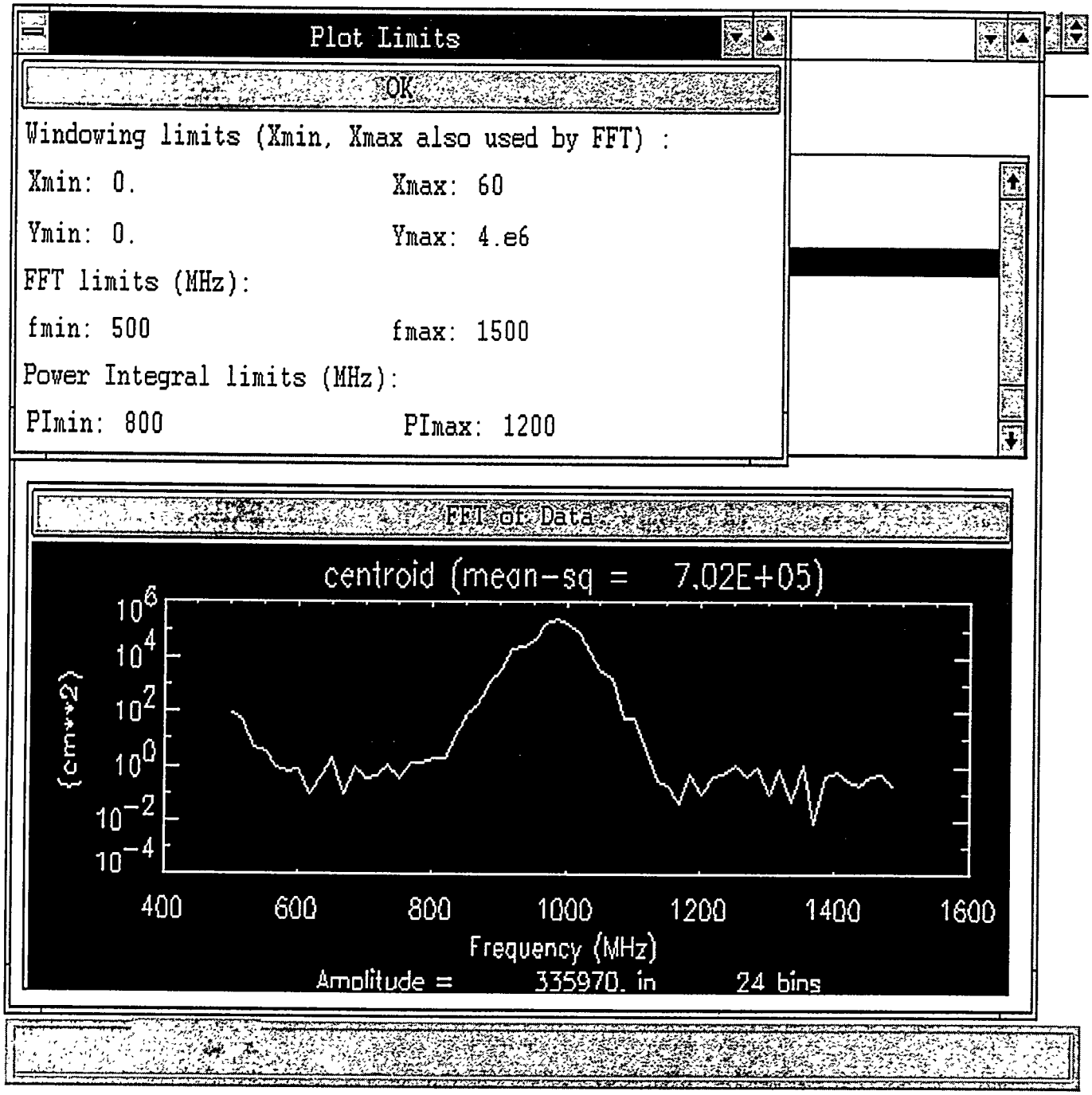

Figure 34. VIEW display showing windowing dialog box on top and the FFT of data in Fig. 33 on bottom.

Ref. 15, Sec. 5). As Fig. 34 shows, the windowing box allows one to specify frequency ranges for a "Power Integral". The spectral power is summed over this range, and the square root of this sum is displayed at the bottom of the FFT plot (Fig. 34).

The Postscript hard copy obtained for the graph in Fig. 34 (via the "File" button) is shown in Fig. 35.

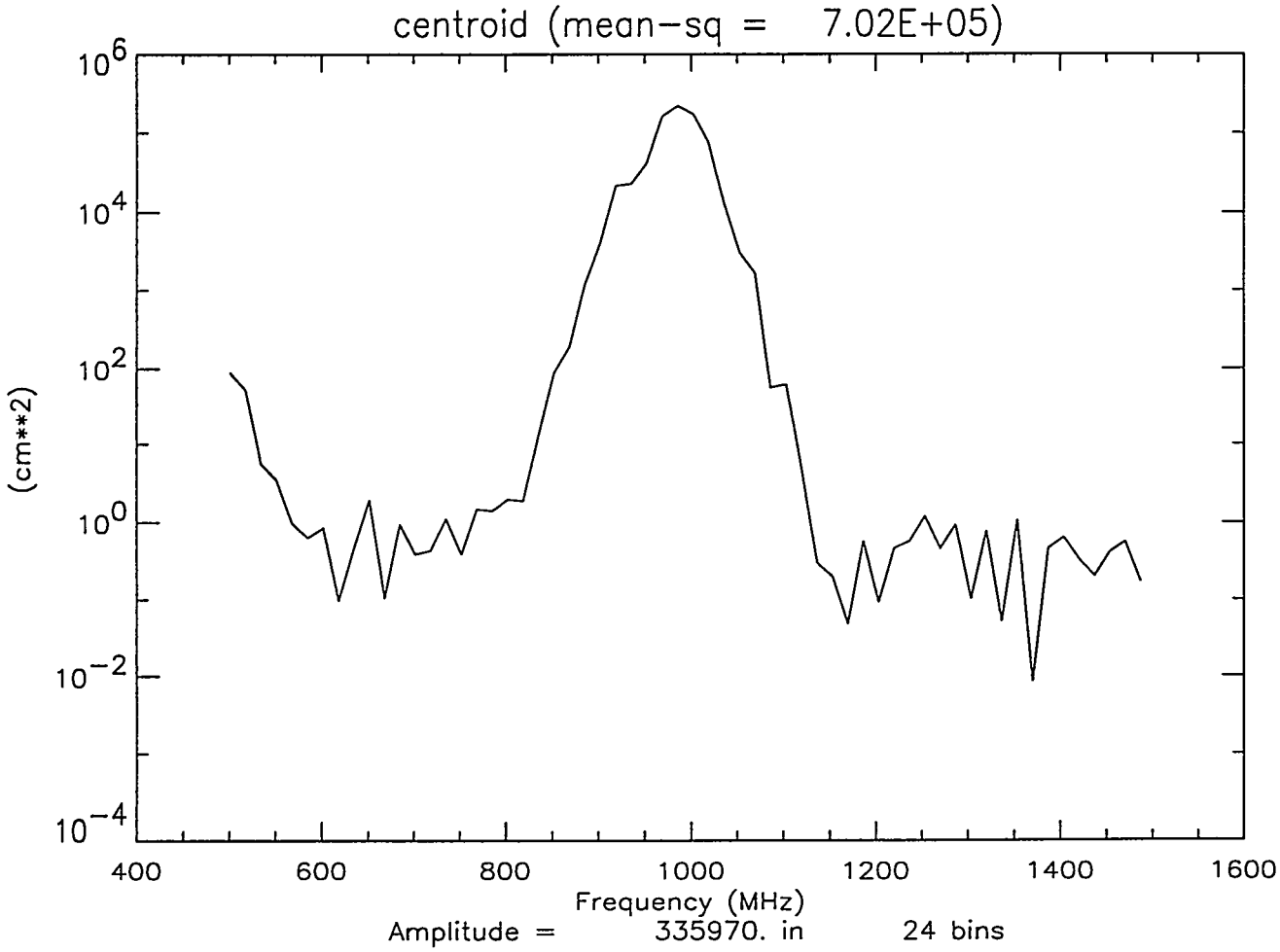

Figure 35. Postscript hard copy of plot in Fig. 34.

REFERENCES

1. BTEC was derived from the SOS code, and is maintained by Bob Clark at Mission Research Corporation.

2. T. P. Hughes and R. E. Clark, MRC Memo, December 6, 1993.

3. M. J. Browman, AT-7:93-ATN-18, October 28, 1993.

4. P. Allison, private communication.

5. M. J. Burns, DARHT Technical Note No. 2, December 10, 1990.

6. R. L. Gluckstern and R. K. Cooper, AT-7 Memo, August 4, 1993.

7. DARHT 3.0" Target 6-Way Cross, Drawing No. 47Y274755.

8. PBGUNS (formerly SPEED) was written by J. E. Boers, Thunderbird Simulations, Inc.

9. T. P. Hughes, R. L. Carlson, and D. C. Moir, "Calculations for PIXY, ECTOR, REX, ITS, and TGX," MRC/ABQ-R-1483, Mission Research Corporation, 1992.

10. B. Kulke, "Validation of the BBU Code Against LANL/DARHT Experimental Data," LLNL Memo, LDD 93-38, October 11, 1993.

11. T. P. Hughes, D. R. Welch, R. L. Carlson, T. J. Kauppila, and D. C. Moir, "Computational Support for ITS, ECTOR, PIXY, and PHERMEX," MRC/ABQ-R-1609, Mission Research Corporation, April 1990.

12. T. P. Hughes, R. M. Clark, R. L. Carlson, and D. C. Moir, "PHERMEX, REX, and Thomson-Generated XUV Calculations," MRC/ABQ-R-1391, Mission Research Corporation, April 1991.

13. D. Venable, D. O. Dickman, J. N. Hardwick, E. D. Bush, Jr., R. W. Taylor, T. J. Boyd, J. R. Ruhe, E. J. Schneider, B. T. Rogers, and H. G. Worstell, "PHERMEX: A Pulsed High-Energy Radiographic Machine Emitting X-Rays," LA-3241, Los Alamos Scientific Laboratory, 1967.

14. W. H. Press, B. P. Flannery, S. A. Teukolsky, and W. T. Vetterling, "Numerical Recipes: The Art of Scientific Computing (Fortran Version)," (Cambridge University Press, New York, 1989).

15. T. P. Hughes, R. M. Clark, T. C. Genoni, and M. A. Mostrom, "LAMDA User's Manual and Documentation," MRC/ABQ-R-1428, Mission Research Corporation, April 1993.

16. IDL Version 3.1, Research Systems, Inc., 1993.

APPENDIX A
ESTIMATE OF LEAKAGE CURRENT

The ferrite block in the accelerating cell acts like a transmission line with a round-trip transit time $\tau_t \equiv 2F\sqrt{\mu\epsilon}/c$, where F is the length of the block and μ, ϵ are the relative permeability and permittivity. The leakage current is simple to calculate in two limits: $\tau_p \leq \tau_t$ and $\tau_p \gg \tau_t$, where τ_p is the accelerating pulse length. In the first case, a step voltage pulse of magnitude V produces a constant leakage current $I_l = V/Z$, where the transmission line impedance Z is given by

$$Z \approx 60\sqrt{\mu/\epsilon}\log\frac{R_{\text{outer}}}{R_{\text{inner}}} \quad \Omega \tag{A.1}$$

where R_{outer}, R_{inner}, are the outer and inner radii of the ferrite core, respectively. Taking $R_{\text{outer}} = 25.2$ cm, $R_{\text{inner}} = 11.5$ cm, $\mu = 230$, and $\epsilon = 3$, we find $Z \approx 412\ \Omega$. For a 250 kV accelerating voltage, this gives a leakage current of 607 A for a period $\tau_t \approx 53$ ns.

In the limit $\tau_p \gg \tau_t$, the cores act like a lumped impedance of magnitude

$$L \approx 2 \times 10^{-7}\mu\ F\log\frac{R_{\text{outer}}}{R_{\text{inner}}} \quad \text{Henry} \tag{A.2}$$

A simplified equivalent circuit is shown in Fig. A–1. The leakage current evolves approximately according to

$$I_l = \frac{Vt}{L} \tag{A.3}$$

where V is the accelerating voltage and t is time. Taking $R_{\text{outer}} = 25.2$ cm, $R_{\text{inner}} = 11.5$ cm, $F = 30$ cm, and $\mu = 230$, we find $L \approx 10.8\ \mu$H. For these numbers, the lumped impedance model is valid only for pulse times much longer than $\tau_t \approx 53$ ns. It gives a leakage current rise of 23 A/ns for $V = 250$ kV.

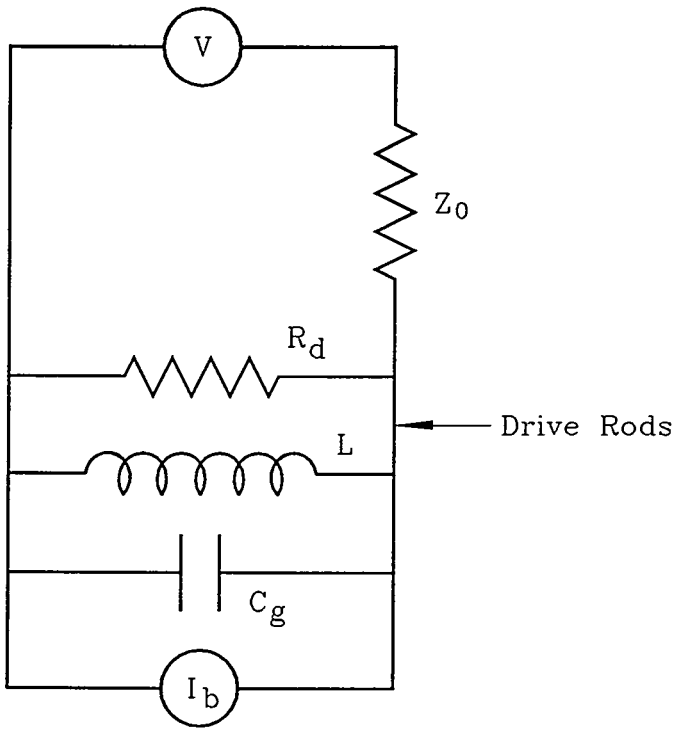

Figure A–1. Simplified equivalent circuit for accelerating gap, with a damping resistor (R_d), core inductance (L), and gap capacitance (C_g). During the flat-top of the beam pulse, the drive rods conduct the sum of the leakage current and the beam current.

APPENDIX B

BFIELD INPUT FOR ITS DIODE MAGNETS

The following is the DATA1 file which BFIELD reads to get the coil configuration for the PBGUNS simulation in Sec. 2.3. The third and fourth lines contain the bucking coil and anode coil, respectively. The axial coil location (z_1 to z_2) is given with respect to the non-emitting cathode electrode. The last two lines give the two-dimensional region over which the field is to be generated. The axial region starts at -2.0 cm because in PBGUNS, the cathode plane is 2 cm from the start of the mesh (see Fig. B–1).

```
0
2       Number of coils following
-19.26 92.0 95.0 -23.0 -8.0 1 1      (Amps, r1, r2, z1, z2, Nr, Nz)
170.0 9.47 10.82  34.12 82.58 3 40
0.0
1
0.0 1.0 150 0.0 3.0 1 1
1
0.0 25.0 1 0.0 0.5 16 1
1
3 3
1.0 55.5 -0.5 110
3.0 55.5 -0.5 110
5.0 55.5 -0.5 110
1
3.0e10
-2.0 80.5       Axial region
0.0 7.5         Radial region
```

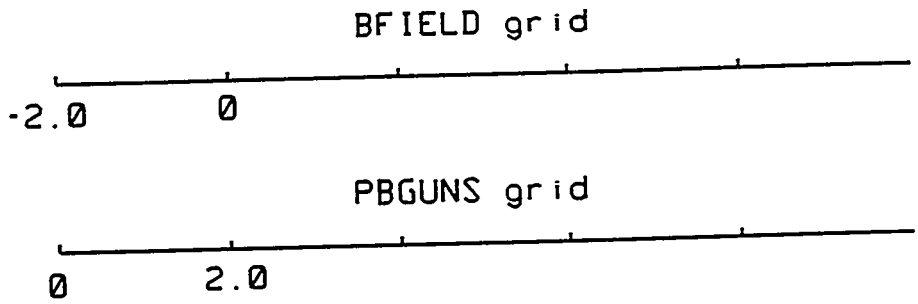

Figure B–1. Origin of coordinate system for BFIELD input data is at the non-emitting cathode plane. Since PBGUNS mesh must start at zero, the cathode surface is at $z = 2$ cm in PBGUNS in this example.